Science Advances
AAAS

Supplementary Materials for

A fully integrated breathable haptic textile

Kuanming Yao *et al.*

Corresponding author: Zijian Zheng, tczzheng@polyu.edu.hk; Xinge Yu, xingeyu@cityu.edu.hk

Sci. Adv. **10**, eadq9575 (2024)
DOI: 10.1126/sciadv.adq9575

The PDF file includes:

Texts S1 to S6
Tables S1 and S2
Figs. S1 to S34
Legends for movies S1 to S5
References

Other Supplementary Material for this manuscript includes the following:

Movies S1 to S5

Supplementary Text

Text S1: The effect of sweating and breathability on the hand and on wearable haptic interfaces

Breathability is essential to the wearable haptic interfaces, and a well breathability will result in improved wearing comfort because the sweat is allowed to evaporate from the skin, instead of causing uncomfortable feelings such as irritations, dampness, and clamminess. Here we discuss the underlying mechanisms in detail and point out the necessity of breathability for wearable haptic interfaces, especially for the hand.

For perspiration, in addition to sweating (liquid droplets), there's also insensible perspiration, i.e. passive transepidermal water loss (TEWL). The difference between these two modes is embodied in the rapidly increasing evaporation rate from the whole body when the ambient temperature is transitioned from 31 °C to 34 °C.(*37*) When there's skin occlusion that caused by unbreathable clothing/gloves/dressings, this sweating-facilitated thermal equilibrium is impeded severely, thus the local temperature and humidity are also increased and further enhances the sweating, which may turn insensible perspiration into sweating even in normal ambient temperature. As the skin functions as the barrier between external and internal environments, the skin occlusion would lead to enhanced stratum corneum hydration and reduce the barrier efficiency.(*35*) Because of the increased stratum corneum hydration, the swelling of corneocytes would lead to promoted water absorption in intercellular lipid domains, as well as promoted penetration of lipid-soluble nonpolar chemicals. Thus, the applied compounds would have aggravated irritations to the skin and result in contact dermatitis.

As the skin on hands/fingers has the densest distribution of sweat glands(*51*), the perspiration rate there is also one of the highest (comparable to axilla and sole) across the human body. Thus, ensuring a well-ventilated environment around the hand/fingers is essential for the health of the skin. Previous studies have found that microclimate changes inside an unbreathable occupational glove would have significant impacts on the skin conductance as well as on perceived discomfort(*38*). Finger and hand pain, erythema and onycholysis frequently occur in occupational gloves (e.g., extra vehicular activity gloves for astronauts). As the skin conductance reflects the amount of hand perspiration and moisture, researchers summarized the results according to the skin conductance changes with three different varying factors, which are ambient temperature, humidity, and exertion strength. Higher temperatures and higher humidity lead to significantly higher skin conductance and higher discomfort level, and exercising is also the same. Higher temperatures within the glove further pronounces the discomfort during exercise, and what's worse is that this temperature increase could be caused by physical exercise-produced metabolic heat. Thus, to keep the hand comfortable during exercising, it's extremely important to maintain well cooling conditions through ensuring the excellent breathability of the glove.

For wearable haptic interfaces, the breathability performance is usually neglected in their designs for ensuring the functionality of haptic feedback. However, the breathability itself will also affect the haptic feedback performance, either by sweat impeding the feedback perception or detaching the interface due to sweat-reduced adhesion. Currently, typical systems are relying on stable and impermeable substances, such as PCBs, leathers, polyimides (PI), and elastomers/rubbers such as PDMS and SEBS. The mechanical actuators require moving structures which should be well encapsulated (which makes it pretty thick), pneumatic/microfluidic actuators require sealed air pipes/microchannels, and thus are both typically impermeable. In contrast, electrotactile haptic feedback only requires routed electrodes that contact the skin well, so they can be built on permeable substrates easily. However, as the hydrogel is adopted in FIBHT to ensure a stable electrode-skin interface, the hydrogel piece-covered small area of the skin is wetted. Thus, the breathability of the inter-electrodes area must be good enough to compensate for the loss of these areas and keep a normal thermal equilibrium for the whole covered area. Otherwise, the increased skin conductance could make the stimulation current density less focused on the local spot and subsequently induce weaker and vaguer perceptions. In most soft wearable haptic systems, the feedback interface may be built on textiles that provides well breathability, but the controlling circuit is still built on rigid PCB/fPCB, PI thin film or intact elastomer film that are impermeable. The main challenge is the lack of precise multi-layer metal circuit patterning and low-temperature soldering technologies on soft and permeable materials. Hence, the permeable three-dimensional circuits manufacturing technology we developed filled in this gap, allowed us to make a highly breathable haptic interface on the hand, which is totally different from other types of haptic gloves that can induce discomfort after wearing for merely several hours.

Text S2: The design of electrodes distribution and densities.

As shown in **fig. S1**, the regional electrodes densities in FIBHT vary according to the parts that have different tactile sensitivity and spatial recognition ability. For fingertips, it's 2.26 pixels/cm^2; for finger phalanges it's 1.41 pixels/cm^2; for MCP joints it's 0.68 pixels/cm^2; for inner palm it's 1.21 pixels/cm^2 and for hypothenar region it's 0.44 pixels/cm^2.

The relative mechanoreceptor innervation density ratio in the palm, finger phalanges (except distal) and fingertip (distal phalanges) is around 1: 1.6: 4.9 (*63*). Thus, in our design, the ratio between regions with highest and lowest electrode densities (fingertip: 2.26 pixels/cm^2 and hypothenar: 0.44 pixels/cm^2) is ~5, and the ratio between fingertip and phalanges (1.41 pixels/cm^2) is ~1.6. According to past and recent literatures, the two point discrimination limen value for fingers are 3~5 mm (*64*), while for inner palm, thenar and hypothenar are basically 11-13 mm (*65*). Thus, in our design, the basic pitch between electrodes at fingers is set to 4.5 mm, and the value in the palm region is between 8~14.5 mm.

Text S3: Comparison between wet hydrogel electrodes and dry electrodes

Typically, there are two types of electrodes for delivering electrical stimulation or electrotactile feedback, which are wet electrodes and dry electrodes according to whether it contains water or not. Metal thin film and pastes (e.g., Au(*26*), Ag/AgCl pastes(*27*), etc.), conducting polymers (e.g. PEDOT: PSS(*66*)), nanomaterials and their composites (e.g. carbon nanotube and graphene-based composites, silver nanowire composites, etc.) could be classified into dry electrodes. In such dry electrodes, electron transportation is the dominant mechanism of electrical conductivity, and thus could reach a much higher intrinsic conductance than wet electrodes. Conductive gels (formless viscid semifluid, such as water/gelatin mixture), hydrogels (PAAm, PAAc, PVA, etc.) that contain ionic electrolytes in the water can be classified into wet electrodes. Hydrogels that have crosslinked or entangled long-chain polymer matrix as the water-entrapping scaffold could maintain certain shape but could also be highly deformable, which endows it tissue-like softness. Besides, ion transportation in the electrolyte is the main contributor to the electrical conductivity. Electricity to be delivered from electronic conductive systems into ionic conductive biological tissues must experience an electron-ion current transferring process. Basically, despite the lower intrinsic conductance, ionic conductive wet electrodes could work better in such electrostimulation interfaces.

This could be attributed to two reasons. Firstly, when using wet electrodes (hydrogel for example) that contact with electronic systems via a large metal pad, its adhesiveness and diffusing water help to form a large and stable electric double layer (EDL) on the metallic electrode-hydrogel interface, as well as a large EDL capacitance (C_{EDL})(*53*). This allows pulsed electronic charges on the metal side to capacitively couple with ionic charges in the hydrogel. As capacitive non-faradic currents that don't involve electrochemical reactions, the ion species and the concentration won't change. C_{EDL} itself could be considered as a first-order high-pass filter, and thus pulsed currents could easily pass through owing to the lower impedance at higher frequency rather than at DC range. In contrast, dry electrodes directly contact the skin and only form smaller and distributed EDL due to the air gaps in the interface if the electrode is not adhesive and completely conformal to the skin. In such cases, faradic current that gives electrons to (or take from) ions would be dominant to deliver stimulation, which is not preferred in bioelectronic interfaces because it will accelerate the corrosion of the electrode or introduce unwanted chemicals into tissues.

Secondly, as skin itself could be considered as electrolytic hydrogel along with little capacitive components (such as stratum corneum), the ionic current could be injected into the skin easily with mainly resistive coupling (R_S) in the intimate hydrogel-skin interface. This resistive impedance could be even further reduced by enhancing the chemical bonding between the hydrogel and the skin, such as the hydrogen bond that contributes to the instant adhesion and covalent bond that contributes to the stable and strong adhesion. As mentioned above, the dry electrode-skin interface possesses poor electron-ion transfer efficiency, and also lacks chemical bonding. Thus, in electrical aspect, the wet electrodes are superior to dry electrodes.

However, hydrogel wet electrodes also have their own deficiencies. The water is continuously evaporating from the hydrogel and may lead to reduced conductivity over time. Hygroscopic electrolytes (e.g., LiCl) and glycerol are typically used for retaining water in hydrogel for a longer period. As hydrogel is too sticky, hard to pattern in fine size and thin thickness, complicated manufacturing techniques should be used for achieving high spatial resolution in wet electrodes. In the fabrication of FIBHT, the bioadhesive hydrogel we developed could be screen-printed into small pieces and photocured in situ, which solved this problem for the feedback-compatible resolution.

Text S4: Design, preparation and characterization of bioadhesive hydrogel

We first prepared a novel bioadhesive hydrogel as the interface between human skin and LM. In general, as an ideal bioelectronic-tissue interface, it should have excellent electrical performances for efficient electrical exchange, rigorous mechanical properties for high conformability and maintenance of structural integrity, superior adhesiveness for better electrophysiological conjugation and integration, high anti-bacterial activity for local infection prevention. In this study, we have developed a bioadhesive hydrogel as the bioelectronic-tissue interface, which is comprised of a complicated double network formed by covalent crosslinking of PAAm and multiple tannic acid (TA)-mediated dynamic interactions (e.g., hydrogen bonds, electrostatic interactions, and Schiff-base/Michael addition reaction). In this system, PAAm-consisted covalent network was used as the main matrix, and other biocompatible components were used as the functional additives, such as sodium chloride (NaCl) for ionic conductivity, sodium citrate for metal interaction, PAAm for enhanced bioadhesion, TA for improved mechanical and adhesive performances, and water-glycerol binary solvent system for long-term application stability.

We first used the Fourier transformed infrared (FTIR) spectrometer to evaluate the chemical composition of the proposed hydrogel. As shown in **fig. S7**, a characteristic broad peak around 3300 cm^{-1} was observed, indicating the presence of intermolecular hydrogen bonding. Distinct bands were also detected at wavenumbers of 2867 cm^{-1} and 2928 cm^{-1}, corresponding to symmetric CH_2 stretching and asymmetric CH_3 stretching, respectively. The peak at 1650 cm^{-1} was ascribed to the C=O stretching of ester groups in hydrogels, while the absorption peaks at 1601 cm^{-1} and 1450 cm^{-1} were associated with the stretching vibrations of the aromatic ring (C=C). In addition, the peak at 1040 cm^{-1} was attributed to symmetric C-O stretching of ether group in hydrogel. These results demonstrated the successful introduction of various functional components like PAAm and TA, and indicated the existence of multiple molecular interactions within the hydrogel matrix. Next, scanning electron microscope (SEM) was performed (**fig. S8 a~b**), and we found that such hydrogel possessed microporous structure. In the context of an electrical bio-adhesive interface, a moderate swelling property is considered a prerequisite for its optimal physical performance. Prior research has indicated that the interface hydrogel should exhibit rapid absorption of interfacial water to enhance tissue bonding. However, it is important to prevent excessive swelling under highly humid environments, as this can potentially compromise the structural stability and mechanical performance of the hydrogel(*49*). The swelling ratios of bioadhesive hydrogel after immersion in PBS for 12, 24 and 48 h are displayed in **fig. S8D**. It was found that the swelling ratio of bioadhesive hydrogel was significantly lower than that of commercial gel patch (Bestpad, Shenzhen) at different time points (133.25 versus 282.89 at 12 h; 201.45 versus 444.87 at 24 h, 251.53 versus 702.66 at 48 h, respectively). With the extension of incubation time, the swelling degree of bioadhesive hydrogel increased more slowly as compared with commercial gel. Such behaviour might be attributed to high crosslinking density of hydrogel network, which enables it to withstand deformation caused by water contact and maintain the structural integrity. Moreover, the *in vitro* anti-dehydration test showed that the loss weight of both bioadhesive hydrogel and commercial gel patch did not exceed 30% after storing for 120 h at temperature of 37°C and humidity of 45% (**fig. S8C**). The exceptional anti-drying performance can be due to the robust hydrogen bonding interactions between glycerol and water, effectively impeding water evaporation.

We further characterized the electrical performance of bioadhesive hydrogel (**fig. S15**). As there are multiple bonding mechanisms between bioadhesive hydrogel and both skin and EGaIn, the hydrogel interfaces with these surfaces are both very intimate and stable, therefore eliminating the gaps that impedes the electrical conductivity, and much lowered the interfacial impedance. The total skin-electrode impedance is measured in multiple conditions including different electrode sizes and materials (bioadhesive hydrogel in both static and 100% stretched state, commercial gel and gold). We found that the impedance is closely related to the size, and larger ones result in lower impedance. Also, the impedance difference between Au and bioadhesive hydrogel is more pronounced in smaller electrode size. In all sizes, bioadhesive hydrogel presents the lowest impedance compared to other ones, and the stretching doesn't have much impact on it. To intuitively compare the impedances between these groups, we took the impedances of a characteristic frequency of 1 kHz, and found the gels all presents impedances lower than 100 kΩ while Au electrodes could achieve over 300 kΩ. Regarding the maximum voltage that could be provided by the control circuit is 135 V, we calculated the maximum current intensity (I_{max_1kHz}) that is allowed to flow through the skin with these impedances accordingly. The result showed that the average I_{max_1kHz} for hydrogels of Φ 2, 4 and 6 mm reaches 2.28, 3.20 and 6.97 mA, respectively, which are already much higher than the needed intensity for electrotactile feedback (0 ~ 2 mA) across the whole hand. For stimulation spots on fingertips that requires fine resolution but low current intensity, small pieces (Φ 2 mm) of hydrogel are used. Φ 4 mm pieces are used for where a little higher current is needed but with poorer spatial distinguish ability (MCP knuckles, inner palm). Φ 6 pieces are used for those parts with highest thresholds (thenar and hypothenar).

The mechanical properties of skin-device hydrogel interface are of paramount importance in its practical application. Our results demonstrated that the bioadhesive hydrogel possessed comparable tensile modulus (29.9 kPa) to that of native skin tissue, with its maximum tensile strength of ~70 kPa at stain of ~1000% (**fig. S12J-L**). It exhibited sufficient flexibility, strength, and fracture toughness, thus meeting the essential mechanical requirements for serving as an effective interface material for skin tissue. Furthermore, we evaluated the adhesive performances of hydrogel interface by three tests including lap-shear tests, 90° and 180° peel-off tests (**fig. S12**). Both lap-shear tests and 90° peel-off tests revealed that such hydrogels had superior tissue adhesiveness with shear strength of ~23 kPa for 2M, ~21 kPa for 3M, and ~17 kPa for 4M, and peel-off strength of ~110 N/m for 2M, ~80 N/m for 3M, and ~60 N/m for 4M. More importantly, the bioadhesive hydrogel could maintain adhesion (~100 N/m) even after 20 cycles of adhering and stripping, confirming the robust and enduring adhesion (**Fig. 3d**). As illustrated in the schematic (**Fig. 2k**), this excellent tissue adhesiveness may be due to the multiple dynamic interactions (e.g., hydrogen bonds, Schiff-base/Michael addition reaction) and physical entanglement effect (e.g., PAAm polymeric chains) between skin tissue and hydrogel. Simultaneously, the carboxylate groups of sodium citrate and catechol groups of TA could form coordination bonds with the Ga^{3+} and/or In^{3+} of EGaIn(*48*). In addition, we found their adhesive strengths decreased gradually with increasing NaCl concentrations in the hydrogel matrix. This phenomenon can be attributed to the heightened crosslinking density, which restricts the mobility of free polymeric chains and impairs the physical entanglement effects. It is worth emphasizing that the introduction of overmuch NaCl would result in precipitation, which has a detrimental impact on the crosslinking of the hydrogel and subsequently diminishes its mechanical and adhesive properties. In addition, we assessed the adhesive strength of hydrogel to electrospun SBS fiber mat via 180° peel-off tests (**fig. S12 G~H**). We found that the plasma treatment before dropping of hydrogel onto SBS fiber mat could remarkably increase its adhesive strength to fiber mat, possibly due to the increased hydrophilicity of SBS facilitating hydrogel invasion into the fibrous structure of SBS mat. **fig. S12I** further verified our hypothesis; following the peel-off tests, a considerable amount of residual hydrogel was observed on the surface of the fiber mat treated with plasma. In contrast, the surface of the non-plasma treated fiber mat remained smooth.

In addition to the above-mentioned physicochemical properties, bio-interface hydrogel material should possess excellent biocompatibility. As displayed in **fig. S9A**, all bioadhesive hydrogels formulated with different compositions (i.e., 2M, 3M, and 4M) exhibited favourable cytocompatibility, as evidenced by a relative cell viability of over 95% after 3 days of culture (**fig. S8B**) and similar cell proliferation rate to control group (**fig. S9C**). In addition, even after combination with LM, the hydrogel/LM composite displayed negligible cytotoxicity. These results indicated that our FIBHT was able to support cell survival and proliferation, showing good *in vitro* biocompatibility. The direct application of biocompatible hydrogels onto the skin carries the risk of bacterial infection due to the propensity of hydrogels to create a favourable environment for bacterial growth. Thus, we employed *E. coli* (gram-negative bacteria) and *S. aureus* (gram-positive bacteria) as the representative model bacteria, and evaluated the antimicrobial efficacy of bioadhesive hydrogel through the plate count method. As shown in **fig. S10**, the colonies of both *E. coli* and *S. aureus* on the agar plates of bioadhesive hydrogel group were much less than those of control and PAAm groups. Quantitative analysis further confirmed the superior bactericidal effect of bioadhesive hydrogel with an inhibitory rate exceeding 80% on the growth of both *E. coli* and *S. aureus*. Such outstanding bacteriostatic activity could be mainly attributed to the intrinsic anti-microbial effects of the incorporated TA, which has been discussed in detail in other literature(*55*, *57*). Altogether, our bioadhesive hydrogel demonstrated its potential to inhibit infection after deployment onto skin tissue.

Text S5: Assessment of interfacial bonding of LM/hydrogel

As illustrated in **Fig. 2h**, hydrogel precursor solution was dropped onto and then infiltrated into the electrospun fibrous SBS network. After in-situ UV irradiation, the hydrogel was trapped within SBS protective encapsulation layer while stably contacting with the underneath LM layer (**Fig. 2i**). As displayed in the schematic (**Fig. 2k**), our prepared bioadhesive hydrogel can bond with LM by coordination interactions between the carboxylate and catechol groups in hydrogel and the Ga^{3+} and/or In^{3+} ions in LM. First, we used X-ray photoelectron spectroscopy (XPS) to analyze surface chemical composition and bonding. As revealed in **fig. S13A**, in the deconvolved high resolution C 1s spectra of LM/hydrogel composite, the peaks at 285.68 eV (yellow) and 288.05 eV (cyan) corresponding to C-O and C=O were slightly higher, as compared with those in the spectra of pure hydrogel, which indicated interactions between LM and hydrogel. Moreover, the Ga 3d spectrum of LM/hydrogel composite showed two peaks at 20.28 eV (Ga^{3+}, green) and 17.68 eV (Ga^0, purple), which were shifted from 19.28 eV (Ga^{3+}) and 17.18 eV (Ga^{1+}) in the spectrum of pure LM (**fig. S13B**), possibly due to the coordination bonds of Ga^{3+} in LM with the carboxylate and catechol groups in bioadhesive hydrogel (**Fig. 2k**). Also, in the In 4d spectrum of LM/hydrogel composite, there was a peak at 15.88 eV, which is attributed to In^{3+}; whereas, there the corresponding peak observed in the spectrum of pure LM is at 15.28 eV. Likewise, we found the In^0 peaks at 442.78 eV ($3d_{3/2}$, purple) and 450.38 eV ($3d_{5/2}$, green) in the In 3d spectrum of LM/hydrogel composite were changed to 442.28 eV and 449.78 eV in pure LM, respectively (**fig. S13C**). Collectively, these results demonstrated the formation of chemical complexation between the bioadhesive hydrogel and LM, which facilitated the establishment of electrical pathways for long-term and stable interfacing with skin tissues.

For a better visualization of LM-hydrogel bonding, we also monitored the behaviours of EGaIn droplet on the bioadhesive hydrogel during repetitive stretching and releasing of the hydrogel. As shown in **fig. S14A**, when the hydrogel is stretched, the EGaIn droplet is concomitantly deformed and increases its interface area. The droplet, which becomes significantly stretched when the strain of the hydrogel reached ~500%, recovers its initial shape when the strain of the hydrogel is released. This finding demonstrated even under large tensile deformation, LM could maintain stable and effective contact with the hydrogel, indicating its great potential to ensure reliable and consistent interface integrity in real application scenario. This surface reconciliation of LM on deforming hydrogels further verified the strong interactions of bioadhesive hydrogel to native oxide layer of Ga_2O_3 and In_2O_3. In addition, we found that the oLM could form an even better interface with bioadhesive hydrogel (**fig. S14B**). Different from pure EGaIn, the contact angle of oLM is much smaller due to its higher wettability to the hydrogel, and resulted in a much thinner coating of oLM at the LM/hydrogel interface and promoted the usage ratio of the LM for forming such an interface.

Text S6: System design and parameter optimizations

Optimization of the FIBHT format: The performance of non-breathable haptic interfaces on the hand can be seriously influenced by perspiration, leading to reduced wearing comfort, loss of adhesion, and subsequent detachment from the skin and resulting in inconsistent haptic feedback perception. Unstretchable haptic interfaces also have similar problems due to the mismatch in the mechanical properties between the device and the skin. Hence, it's important to achieve both highly permeable and stretchable on the hand-interfaced wearable haptics. To improve the stretchability of the conducting traces, as previously used brittle metal thin film traces require a serpentine-shaped mechanics design to achieve stretchability, thus occupying a larger area than straight lines, intrinsically stretchable materials are needed to increase routing density and array density while ensuring high stretchability. The substrate material of SBS fiber mat was chosen for its excellence in both breathability and stretchability. We initially designed the system in a two-part form which consisted of a hand-shaped electrode array and a flexible circuit board. However, as this system involved a large number of electrodes, requiring more connectors and cables (e.g. flat flexible cable), leading to more severe mechanical mismatch problems in the soft/rigid interfaces. Therefore, a fully integrated form was chosen, unifying the material system of substrate and routing conductor (liquid metal, LM) for both the electrode and circuit parts, eliminating the need for connectors and cables, and enhancing overall wearing comfort and device flexibility to adapt to various hand activities and movements. The entire device, especially the LM routings and electrical components, is fully encapsulated with breathable encapsulation that of the same material as the substrate, ensuring that it is not scratched or short-circuited by skin contact, and that LM does not leak and contaminate the skin surface. The hydrophobicity of the encapsulation material ensures that the device is insensitive to internal/external water droplets, enhancing system stability.

Optimization of adhesion/electrical interface with skin: Ordinary hydrogels (e.g. pure PAAm) are not adhesive enough, which could not adhere tightly to either the substrate or the skin. Therefore, to maintain stable and consistent electrical conductivity in the electrode-skin interface, the requirement of the interfacial material was to adhere to both sides, but with better bonding with the substrate to avoid sticking to the hand and peeling off from the substrate when taking off the device, and good chemical bonding with the liquid metal to ensure large electric double layer capacitance and a low interface impedance. Therefore, the compositions (PAAm, TA, sodium citrate) that can bond with both the skin and the liquid metal were chosen, and a photocurable form was chosen for convenience in fabricating small-sized electrodes with easy screen printing. Considering biocompatibility, the composition in normal saline (NaCl) was chosen as the conductive ionic electrolyte. Experiments were conducted with solution concentrations of 2-4 M, and it was found that at lower concentration (2M), the adhesion with the skin was stronger (**fig. S12**), biocompatibility was better (**fig. S9**), and all electrical performance measured with this concentration was sufficient for effective stimulation (**fig. S15**). Thus, this electrolyte concentration was chosen. The optimized strong skin adhesion, combined with the excellent flexibility of the device matrix, and the light-weight owing to the permeable microfiber mat structure, allows the FIBHT to firmly adhere to the skin surface without hindering movement or exerting obvious force to the hand during various large deformations (**Movie S5**), endowed the entire movement process of the hand more freedom, and reducing the presence feeling of the device on the skin surface.

Fabrication Process Optimization: The original process of patterning LM was the transferring of photolithography patterned-Ag film onto fiber mats and selective wetting of LM, the required photolithography process is not compatible to FIBHT, since its overall size that including hand-shaped electrodes array and control circuit was too large for photolithography. Thus, we chose a large-size PCB manufacturing-compatible process, which is high-precision laser cutting and stencil printing for patterning LM circuits (**fig. S2**), and successfully achieved the preparation of the device with this size. Since the encapsulation layer can protect the LM conductor and meanwhile allow the uncured hydrogel to penetrate and be fixed after curing, this also eliminates the need of cutting the encapsulation for exposing the LM, which makes it much more convenient. Similarly, the paste mask layer (between components and top layer LM traces) also ensures the protection of the LM traces while allowing the oLM paste to penetrate and form the vertical connections, only exposing the pads that need to be soldered. This is crucial when soldering components onto the FIBHT circuit, after patterning the LM circuits, as it efficiently prevents LM from being accidentally scratched and short or open-circuited by the placement of chips and components.

Stimulation Parameter Optimization: Based on previous study, monophasic current pulses of approximately 20-50 Hz and 1~5 % duty cycle can effectively induce electro-tactile sensations. But we also found that after a period of time stimulating with the same parameters, the sensation intensity gradually weakened, as if the nerves connected to the receptor or the brain had become accustomed to this static/repetitive stimulation and no longer responded to it actively. We also found that, in addition to further increasing the current intensity which can reawaken the perceived sensation, introducing a continually changing parameter without increasing current intensity can also maintain the feedback being effectively felt for a longer time and most users can clearly distinguish the differences among various changing modes. This shows that compared to steady-state/static stimulation input, the human body is more sensitive to dynamic changing stimulation input. Therefore, we introduced a spatiotemporal scanning pattern and a dynamic electro-tactile strategy with periodic frequency changes, thereby achieving a higher recognition accuracy for the overall feedback information. Meanwhile, we also found that when the hand presses the electrode hard, trying to lower the impedance and allow current to pass through easier, it is more difficult to feel the electro-tactile stimulation. The reason may be that the sensation input brought by muscle control and external objects overrides the stimulation current to the nerves. On the contrary, when the hand does not touch external objects and maintains a relatively relaxed state, the user reported sensation of stimulation is very clear. Therefore, it also further illustrates that the bio-adhesive electrotactile interface can maintain efficient tactile feedback without external support, which is crucial for ensuring the clarity of user perception.

Table S1. Comparison with other wearable haptic interfaces on hands

Ref.	Number of haptic units	Air Permeability (mm/s)	WVPR (g/m^2/d)	Stretchability (%)	Skin-interface adhesion strength (J/m^2 or N/m)	Recognition accuracy (%)
(*67*)	5	N/A#	N/A	N/A	N/A	87.2
(*14*)	5	N/A (fabric)	N/A (fabric)	N/A (air tubes)	N/A	78.9 (6 ball) ~89.5 (4 ball)
(*32*)	8	N/A	N/A	100	N/A	N/A
(*68*)	15	Bare hand	Bare hand	N/A (wires)	N/A (commercial gel)	93.3
(*34*)	16	N/A	N/A	N/A	N/A	81.7 (9 textures) ~90.5 (4 textures)
(*69*)	16	N/A	187	46	N/A (pressure-sensitive adhesive)	84.4 (intensity) ~100 (position)
(*70*)	23	N/A (textile)	N/A (textile)	N/A	N/A	88.6
(*17*)	24~64	N/A	N/A	N/A	N/A	80.77 (3×3) ~83.75 (2×2)
(*22*)	32	N/A	94.4	20	1	N/A
(*71*)	64	N/A	N/A	~43	N/A	85 (untrained) ~98.3 (trained)
(*72*)	25 (fingertip) 100 (palm)	N/A	N/A	30	N/A (externally fixed)	85 (intensity) ~87 (pattern)
*	128	40.3~46.3	657.9~ 692.1	500	110	89.7 (ST) ~94.2 (TP/TF)§

* Our work (FIBHT)

N/A, not available.

§ ST, spatiotemporal modes. TP, temporal periodic modes. TF, temporal fading modes.

Table S2. Formulations of bioadhesive hydrogels

Samples	Sodium chloride	Sodium citrate	PAAm	TA	AAm	MBAA	LAP	glycerol	Water
	g	g	g	g	g	mg	g	g	mL
2M	0.46	0.5	0.4	0.32	2.5	5	0.18	3	4
3M	0.69	0.5	0.4	0.32	2.5	5	0.18	3	4
4M	0.92	0.5	0.4	0.32	2.5	5	0.18	3	4

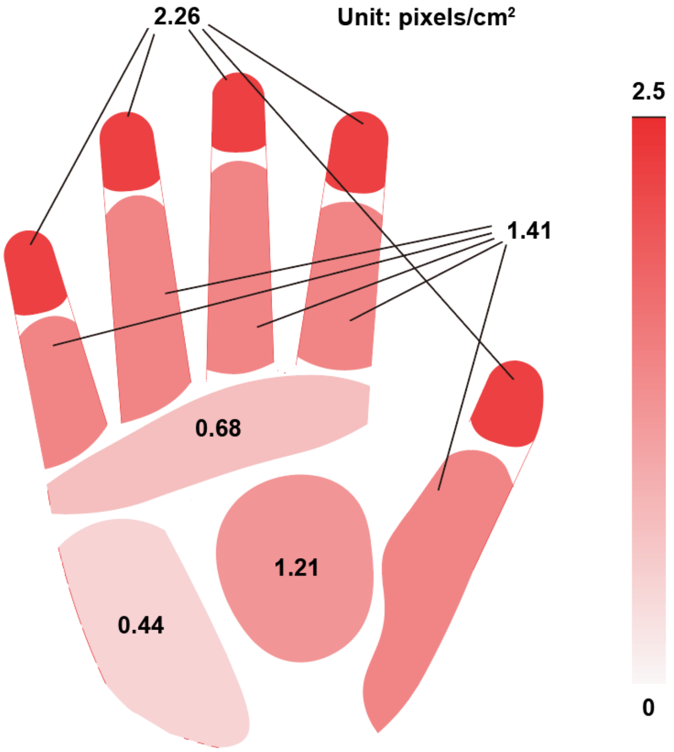

Fig. S1. Pixel density distribution map of the FIBHT.

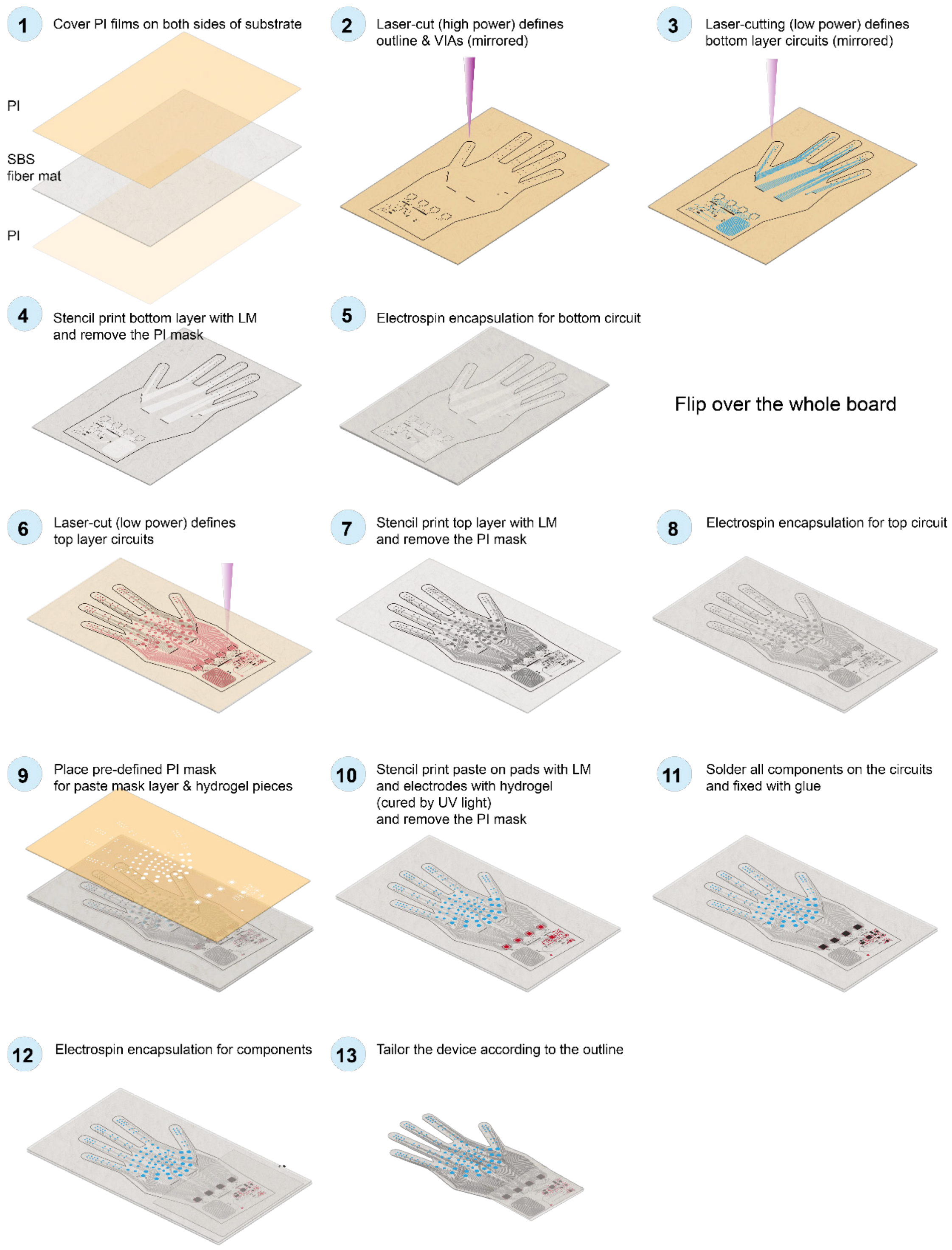

Fig. S2. Fabrication process of FIBHT.

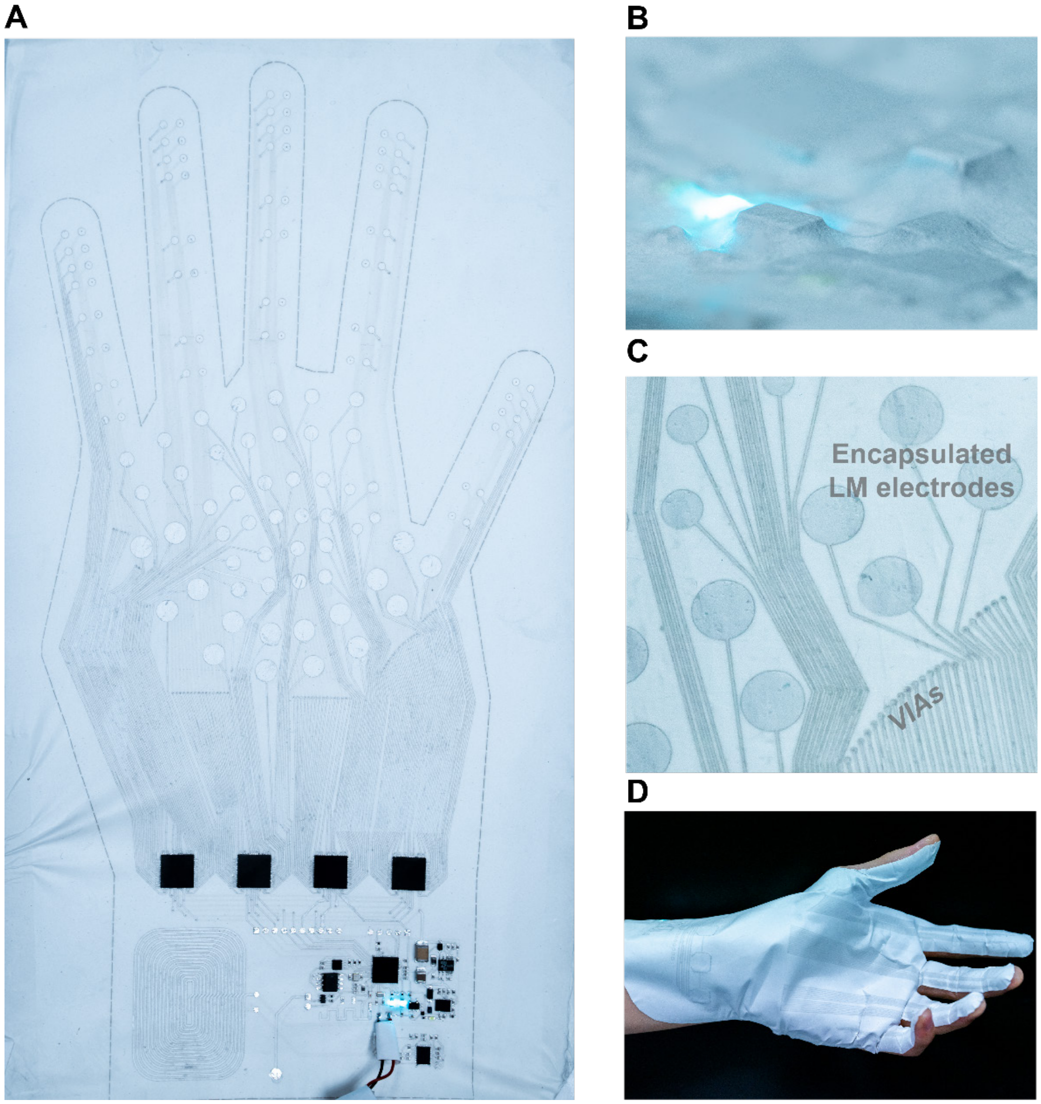

Fig. S3. Supplementary photos of FIBHT and its details. (A), Optical photograph of the assembled but unencapsulated FIBHT system. **(B),** Detailed photograph of the encapsulation over components. **(C),** Detailed photograph of the encapsulated VIAs and LM electrodes. **(D),** Photograph showing a user's hand wearing the FIBHT and posing gesture of shaking hands.

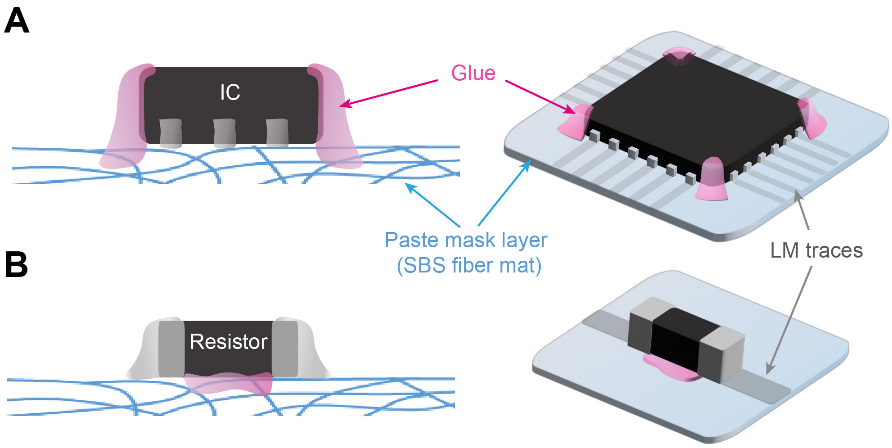

Fig. S4. Fixation methods for electrical components on FIBHT LM circuits. (A), The schematic showing the glue droplet for fixing a surface-mounted IC chip. (**B),** The schematic showing the glue droplet for fixing a surface-mounted resistor or capacitor/inductor. (for both **A** and **B**, left: lateral view, right: perspective view).

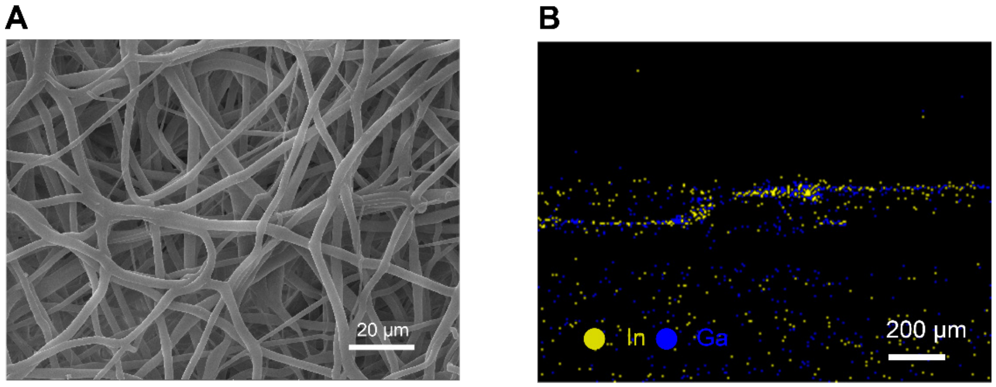

Fig. S5. Morphology and chemical analysis of SBS fiber mat. (A), SEM image of SBS mat. (B), EDX image of the LM, which corresponds to the SEM image in Fig. 2C.

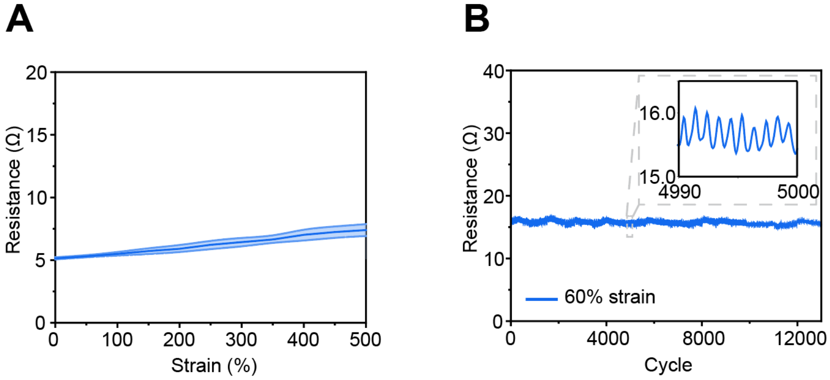

Fig. S6. Stretching tests of long LM traces routed through VIA. (A), Extreme stretching test (length: 10 cm, width: 254 µm). **(B).** Cycled stretching test (length: 15 cm, width: 254 µm).

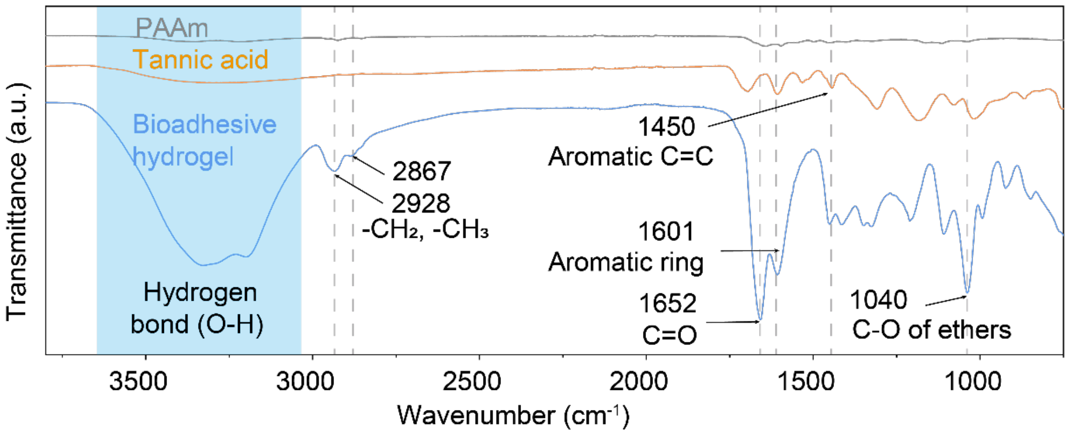

Fig. S7. FTIR analysis of the bioadhesive hydrogel.

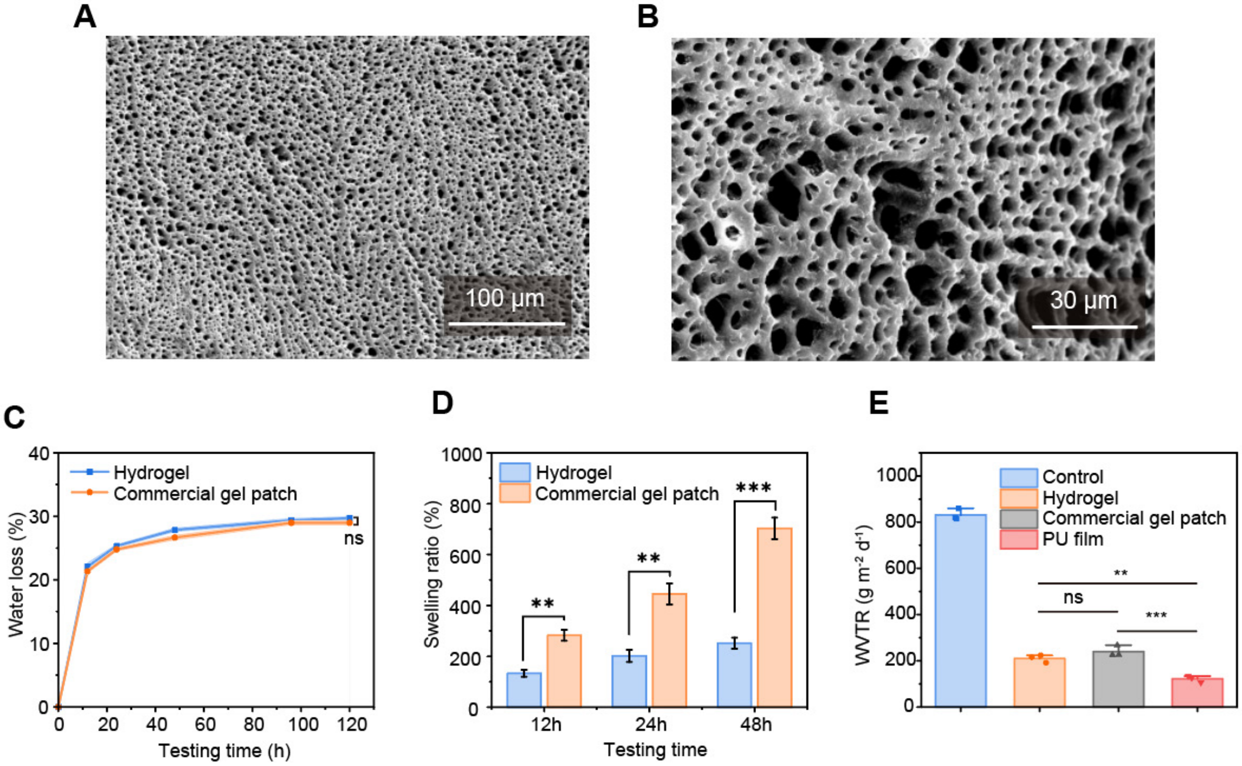

Fig. S8. Characterizations of the hydrogel's morphology and performances. (A), SEM image of the bioadhesive hydrogel. **(B),** Zoomed in detail of a, showing the porous structure. **(C),** Water loss percentage changes of hydrogel and commercial gel patch during 5 days-test. **(D),** Swelling ratios changes of hydrogel and commercial gel patch during 48 hours-test. **(E),** Water vapor transmission rate (WVPR) comparison among bioadhesive hydrogel, commercial gel patch and PU film. n = 3 for **(C)~(E)**. ns denotes not significant, **: $p < 0.01$, ***: $p < 0.001$.

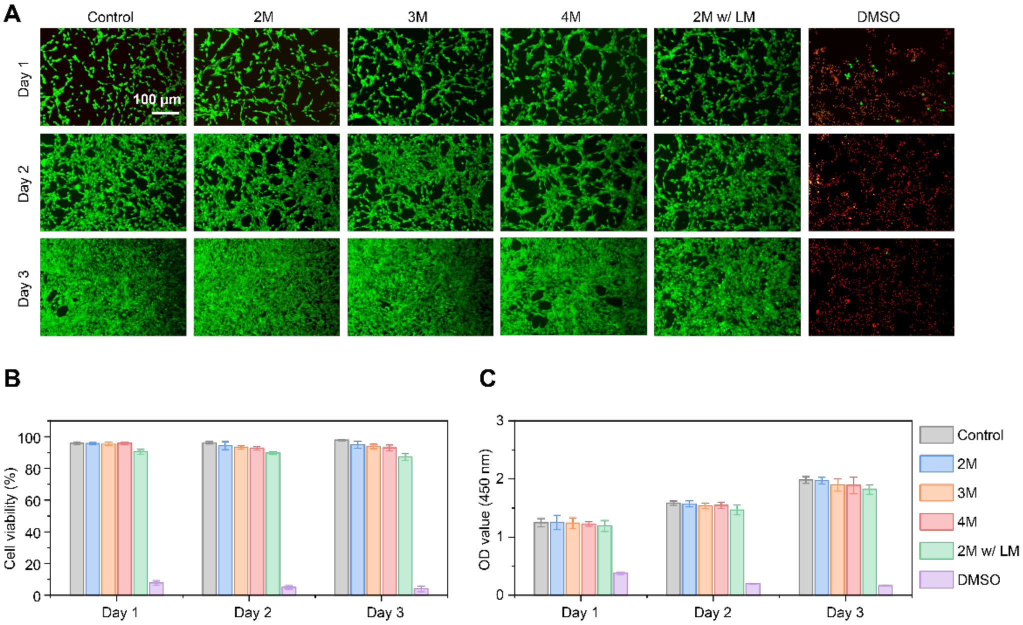

Fig. S9. ***In vitro*** **biocompatibility analysis of the bioadhesive hydrogel. (A).** Live/dead staining of NIH/3T3 cells after culture in different incubation mediums treated with control, 2M, 3M, 4M, 2M+LM, and 20% DMSO. Green fluorescent color represents live cells, while red color indicate dead cells. **(B),** Quantitative evaluation of cell viability in different incubation groups based on Live/dead staining. **(C),** Assessment of cell proliferation after 1, 2, and 3 days of incubation based on CCK-8 assay.

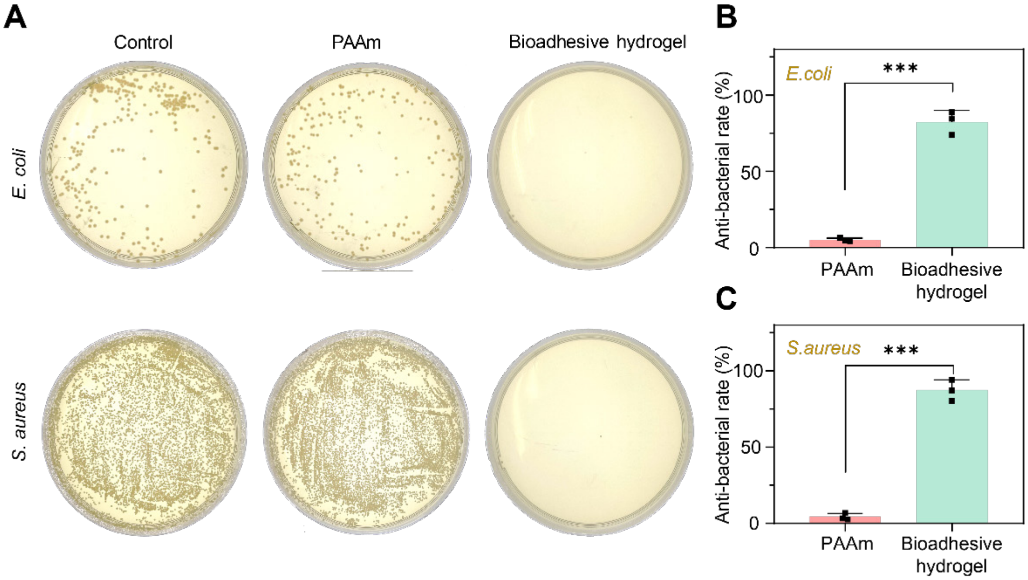

Fig. S10. Assessment of anti-bacterial capacity of bioadhesive hydrogel. (A), Digital images showing the colony formation of *E.coli* and *S.aureus* onto agar plates with different treatments. **(B~C),** Quantitative analysis of the anti-bacterial efficiency of PAAm and bioadhesive hydrogel against **(B)** *E.coli* and **(C)** *S.aureus*. ***, $p < 0.001$ in t-test.

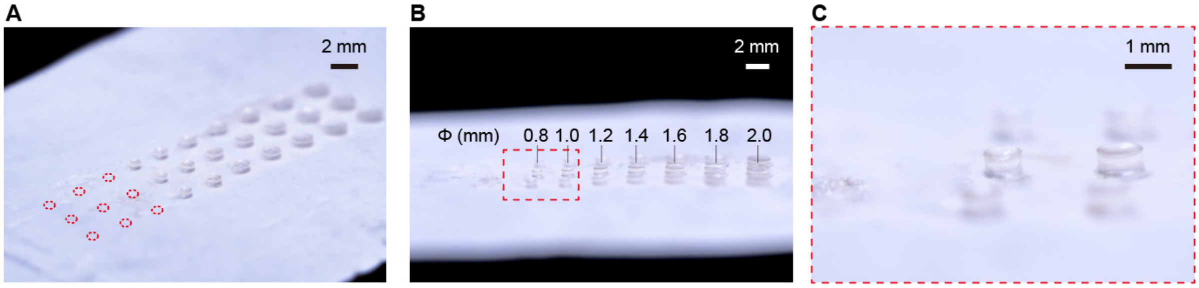

Fig. S11. Minimum achievable resolution test of the photocurable bioadhesive hydrogel. (A-C), Photos of the hydrogel pieces array fabricated by silicone mold-assisted stencil printing and photocuring. **(A):** Perspective view. **(B):** Lateral view. **(C):** Zoomed-in details of Φ 0.8 and Φ 1.0 pieces.

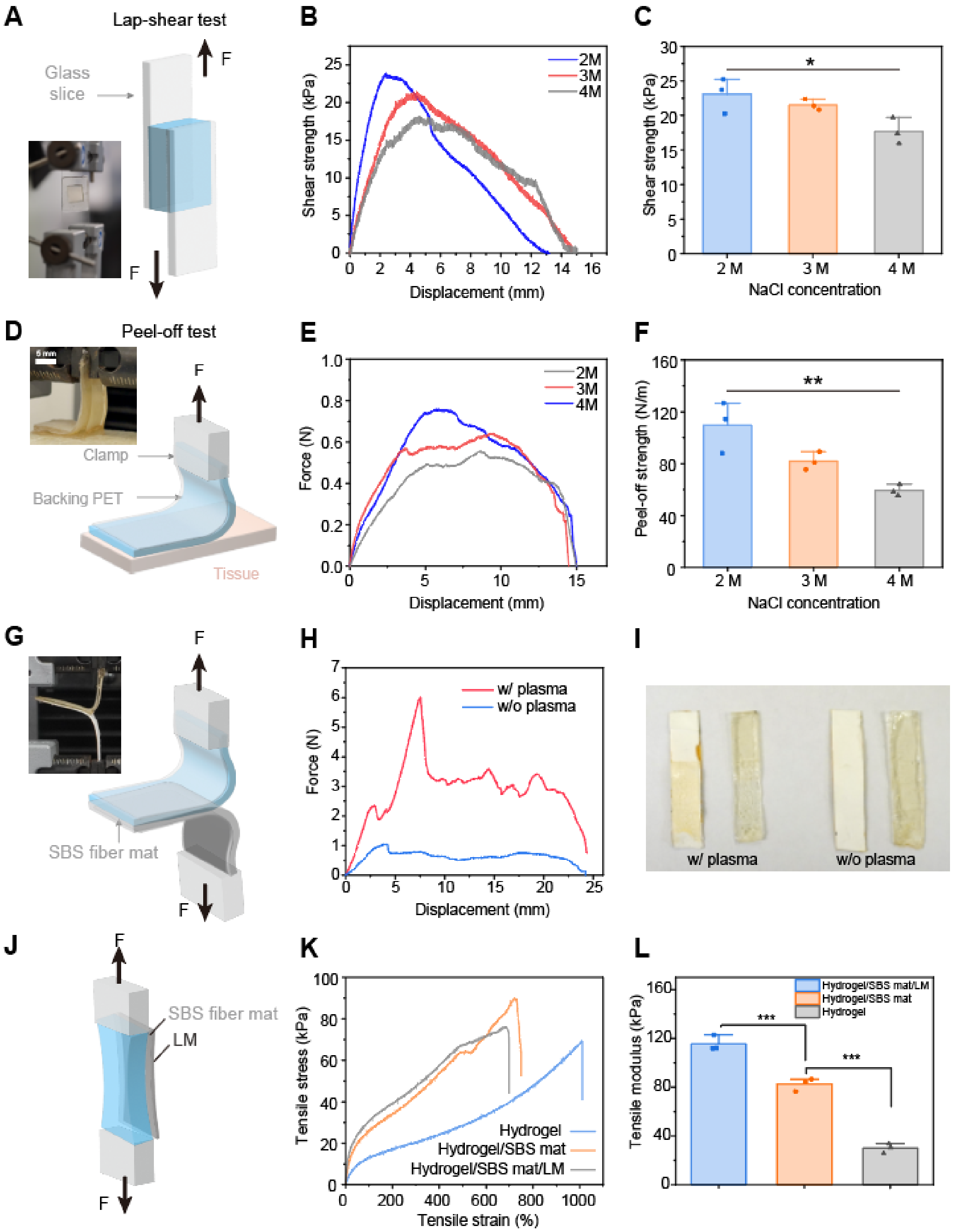

Fig. S12. Mechanical performances of the bioadhesive hydrogel. (A), Schematic illustration and photo of the lap-shear test of bioadhesive hydrogel. **(B),** Shear strength-displacement curves of the hydrogel with 3 different electrolyte concentrations. **(C),** Shear strength comparison among hydrogels with different concentrations. **(D),** Schematic illustration and photo of the peel-off test (90°) for measuring the adhesion strength between bioadhesive hydrogel and tissue surface (porcine skin). **(E),** Peel-off force-displacement curves of hydrogels-tissue interface with different electrolyte concentrations. Electrolyte: NaCl (2~4 mol/L). **(F),** Hydrogel-tissue peel-off strength of 3 electrolyte concentrations. **(G),** Schematic illustration and photo of the peel-off test (180°) of strength between bioadhesive hydrogel and SBS fiber mat. **(H),** Peel-off force-displacement curves of hydrogels-SBS mat interface, with and without plasma treatment for 1 min. **(I).** Photograph showing the hydrogel-SBS mat sample after the peel-off test. Residuals of hydrogel could be observed on SBS samples with plasma treatment, which proved the much stronger interfacial strength. **(J).** Schematic illustration of tensile testing of hydrogel, hydrogel/SBS and hydrogel/SBS/LM composites. **(K).** Stress-strain curves of samples in **(J).** **(L).** Tensile modulus comparison among samples in **(J)** and **(K)**. ns denotes not significant, *: $p < 0.05$, **: $p < 0.01$, ***: $p < 0.001$.

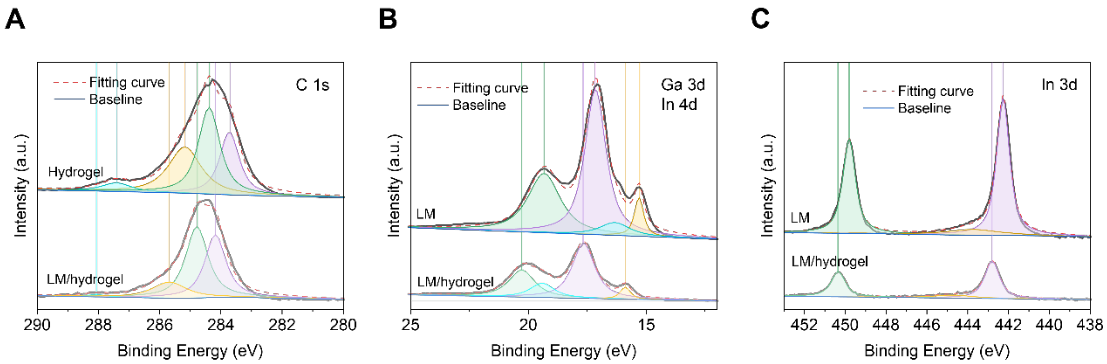

Fig. S13. XPS testing result of the LM-hydrogel interface. (A), C1s spectrum of LM hydrogel and pristine hydrogel. **(B-C),** Spectra of In3d and Ga3d with In4d of LM hydrogel and LM, respectively.

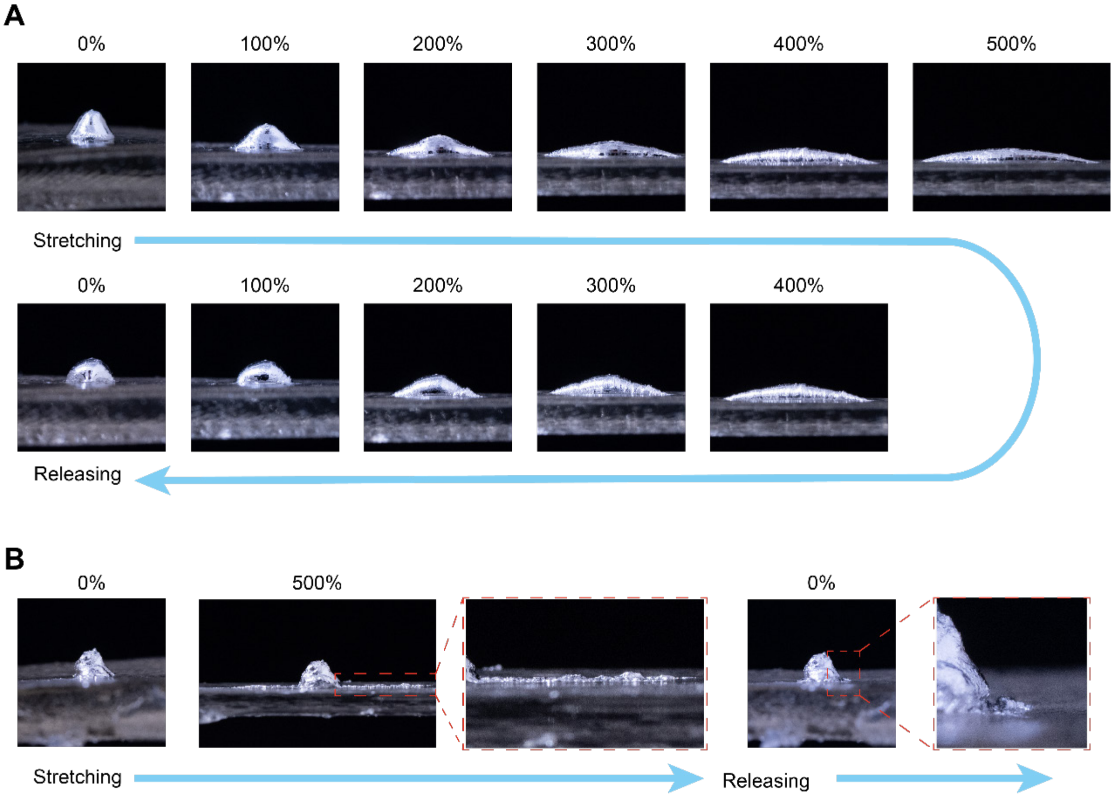

Fig. S14. Characteristics of stable LM-hydrogel bonding. (A), Photographs of EGaIn droplet onto a bioadhevise hydrogel surface during stretch-release process at varying strains. The lengthening shape and decreasing contact angle with growing strain indicated the robust interfacial bonding between LM and the hydrogel. **(B),** Photographs of oLM droplet onto a bioadhesive hydrogel surface during stretching. Different from pure EGaIn, the contact angle is much smaller due to its higher wettability to the hydrogel and resulted in a much thinner coating of oLM at the LM/hydrogel interface.

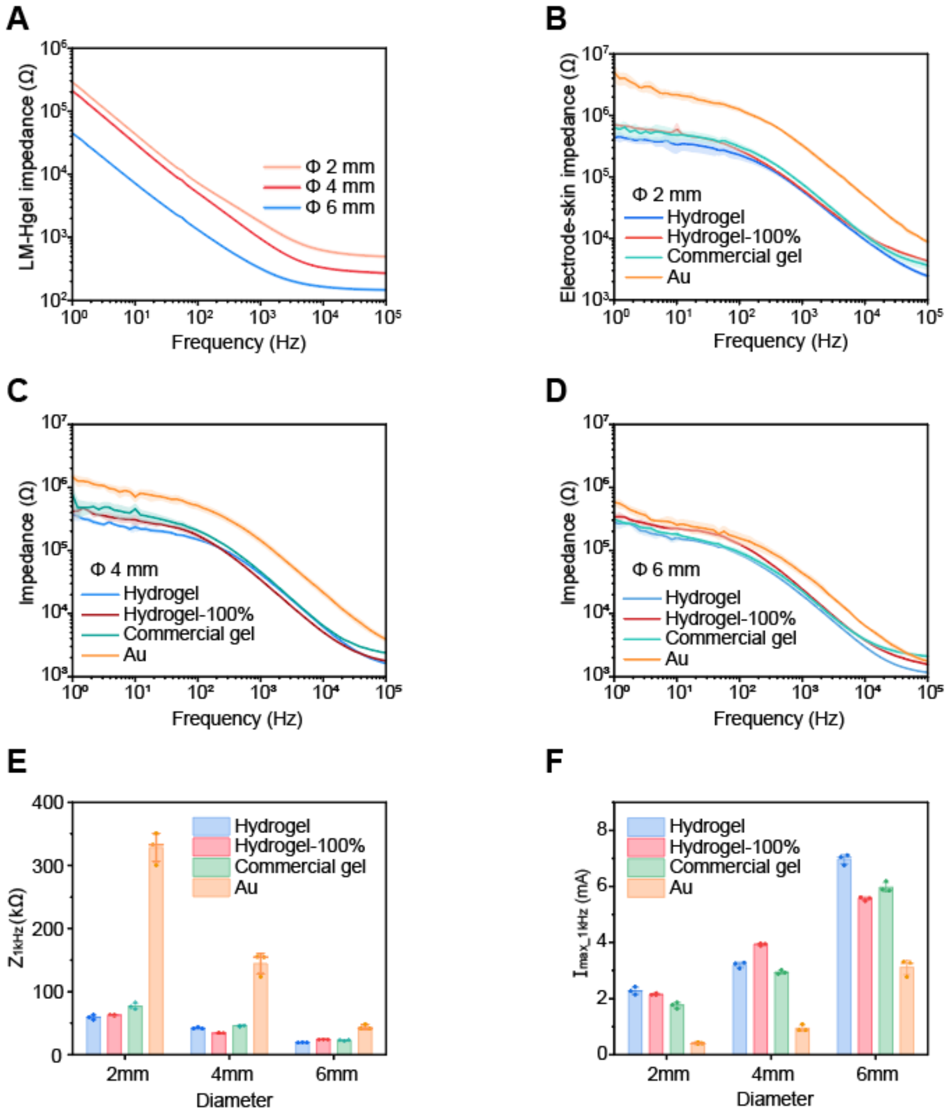

Fig. S15. Electrical performances of the electrode-skin interface. (A), Hydrogel-LM interfacial impedance with different sizes. **(B-D),** Electrode-skin impedance of bioadhesive hydrogel, 100% stretched hydrogel, commercial gel and gold (Au) electrodes, all with a diameter of 2mm (B) 4 mm **(C)** and 6 mm **(D). (E),** Impedances comparison among these electrode materials and among electrode sizes at a characteristic frequency of 1 kHz. Data was extracted from curves in **(B-D)**. **(F),** Maximum current (1 kHz) comparison among these electrode materials and among electrode sizes. Data was calculated from **(E).** n = 3 in each bar and curve. Line & Bar height: mean value. Error bar: S.D. Square, mean; center line, median; box limits, upper and lower quartiles; whiskers, 1.5× interquartile range; points, outliers.

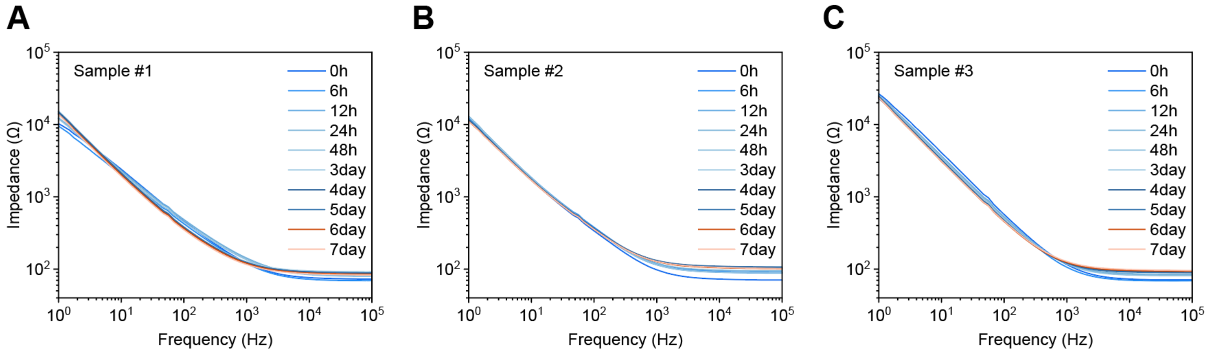

Fig. S16. Long-term impedance test results of the LM-hydrogel interface in 7 days. (A), Sample #1. **(B),** Sample #2**. (C),** Sample #3. Sample size: diameter 6 mm, thickness 1 mm.

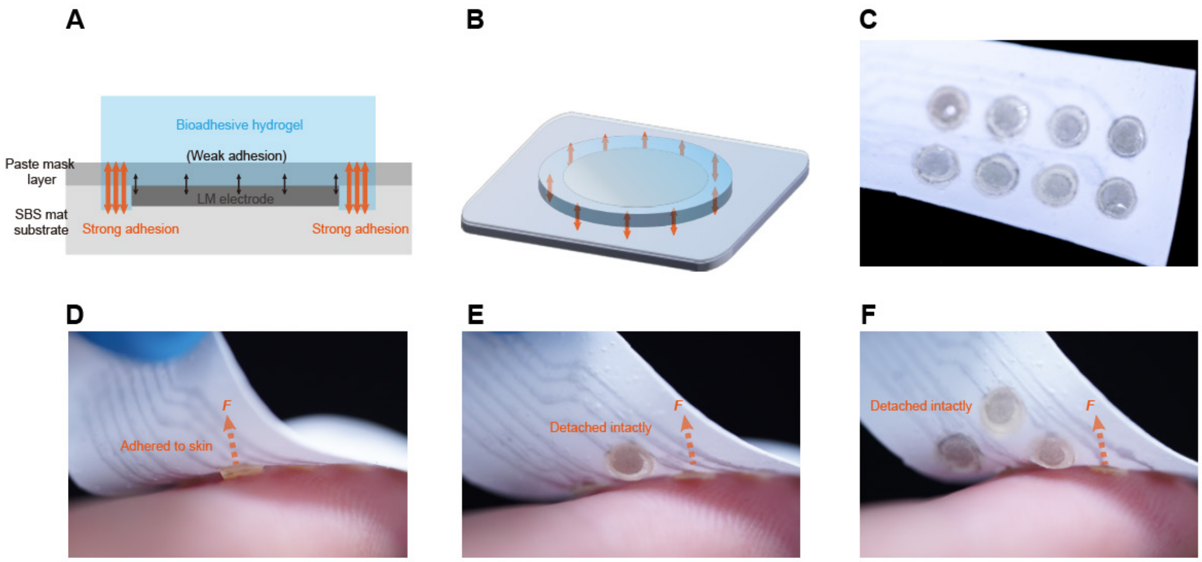

Fig. S17. The architecture for fixing bioadhesive hydrogel and demonstration in detaching from skin. (A-B), Schematic illustration of the fixation architecture (A: cross-section view; B: perspective view). **(C),** Photograph of the hydrogels printed on the finger part of the FIBHT. **(D-F),** Photographs showing the process of bioadhesive hydrogel detaching from the skin when the user peels it off.

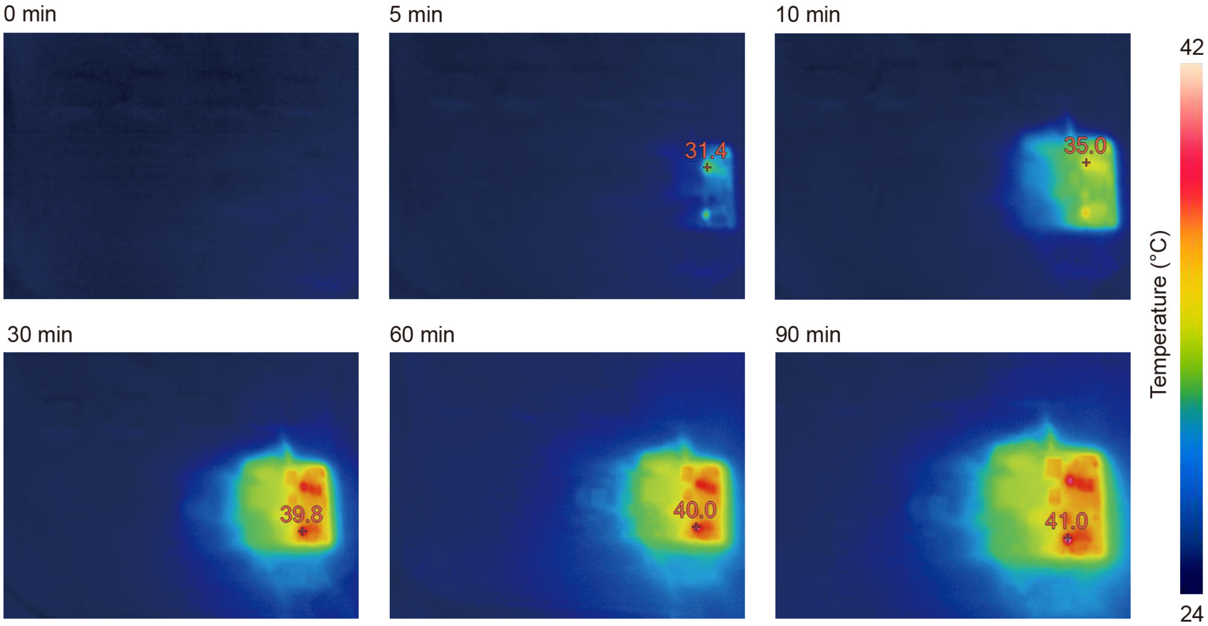

Fig. S18. Heating effect visualization of the control circuit.

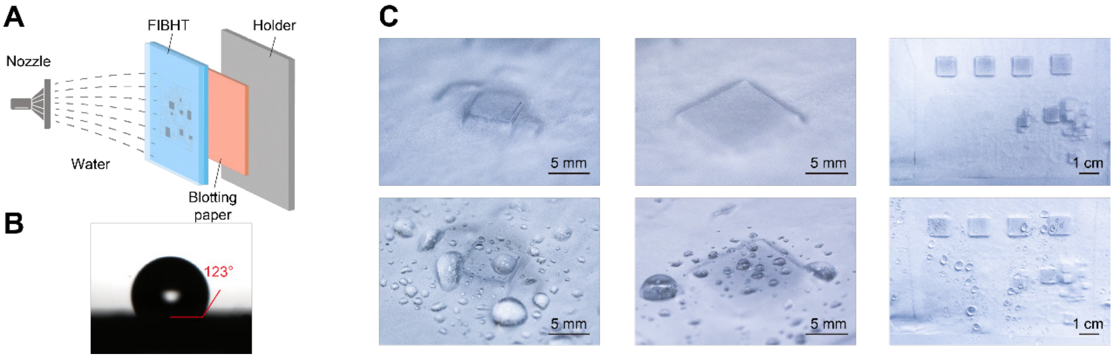

Fig. S19. Waterproof performance characterizations of the FIBHT system. (A), Schematic illustration of the standard rain test (AATCC Test Method 35–2006). **(B),** Photograph showing the water contact angle of the hydrophobic SBS mat. **(C),** Detailed photos of the FIBHT showing comparison between before (upper row) and after (lower row) the rain test.

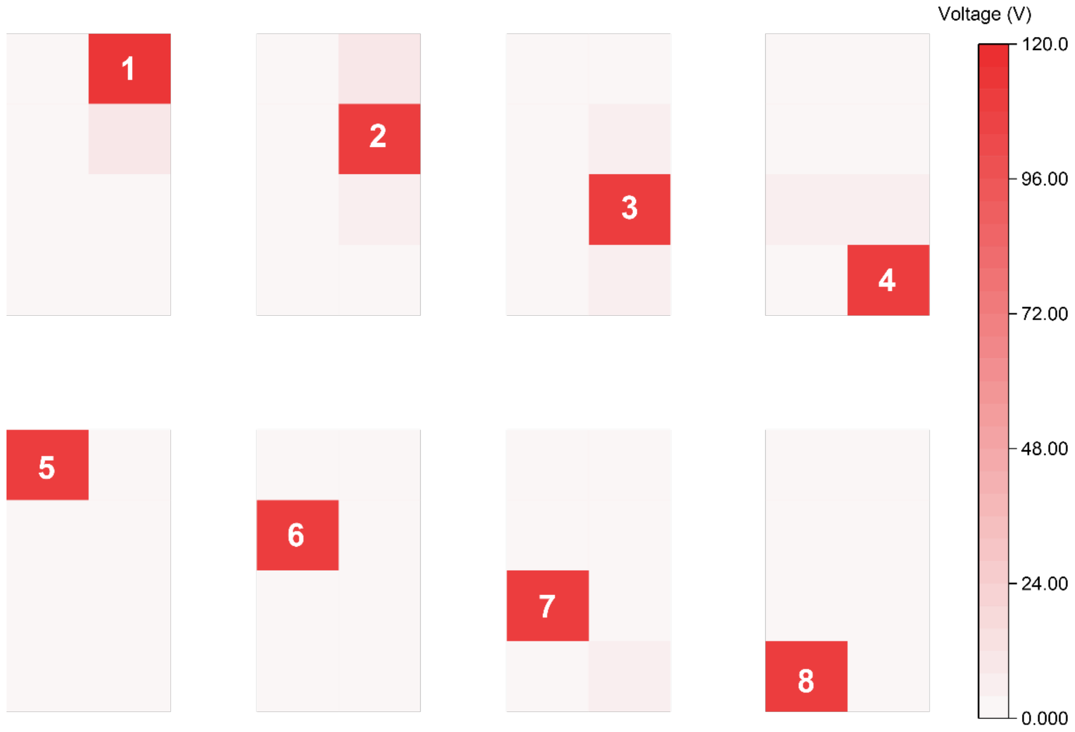

Fig. S20. Crosstalk when **stimulating 1 channel in an 8-channel array.**

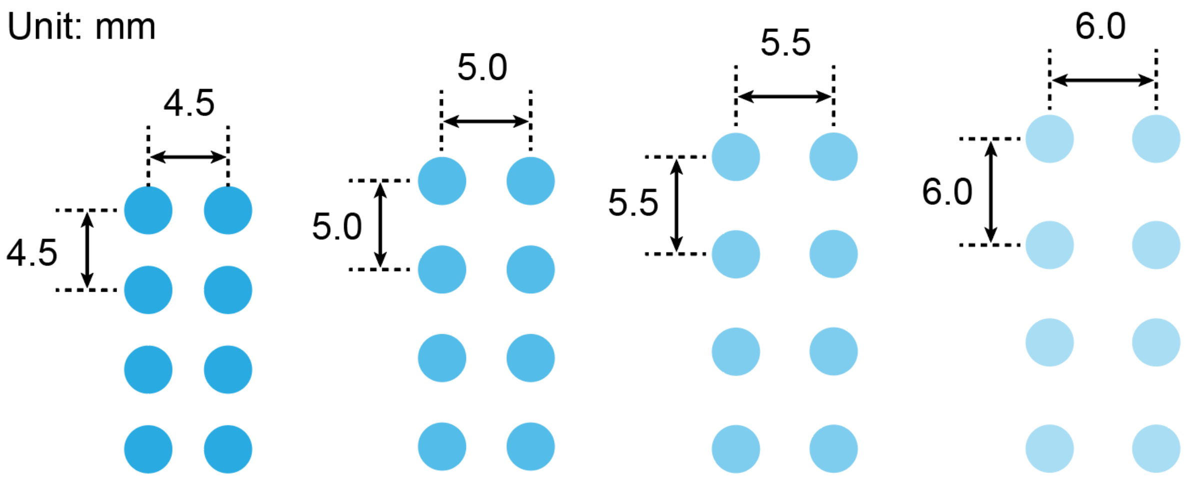

Fig. S21. Designs of fingertip electrodes with varying pitches. From left to right: small (4.5 mm), medium (5.0 mm), large (5.5 mm) and extra-large (6.0 mm).

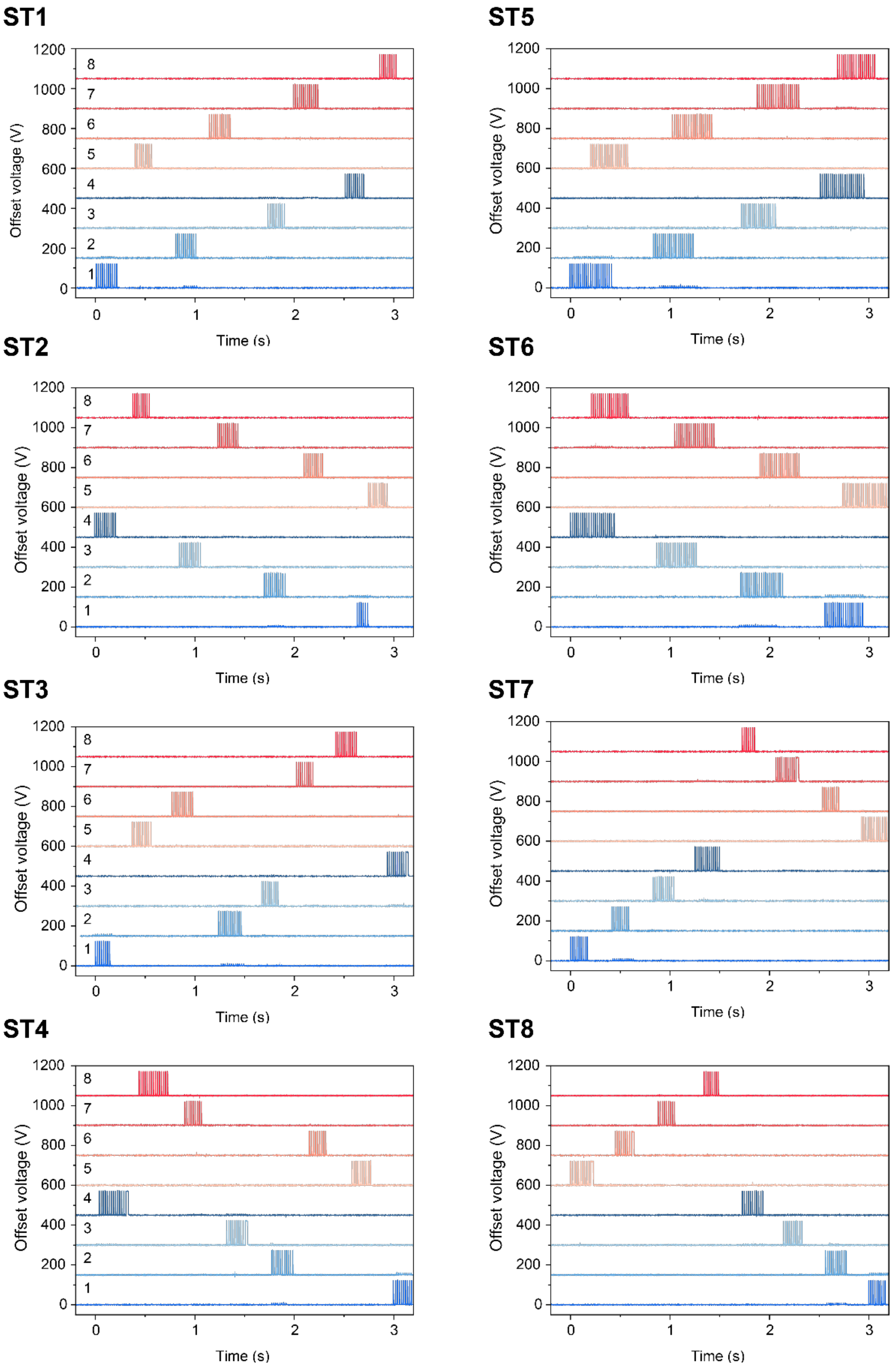

Fig. S22. Time domain plot of dynamic modes ST 1~8.

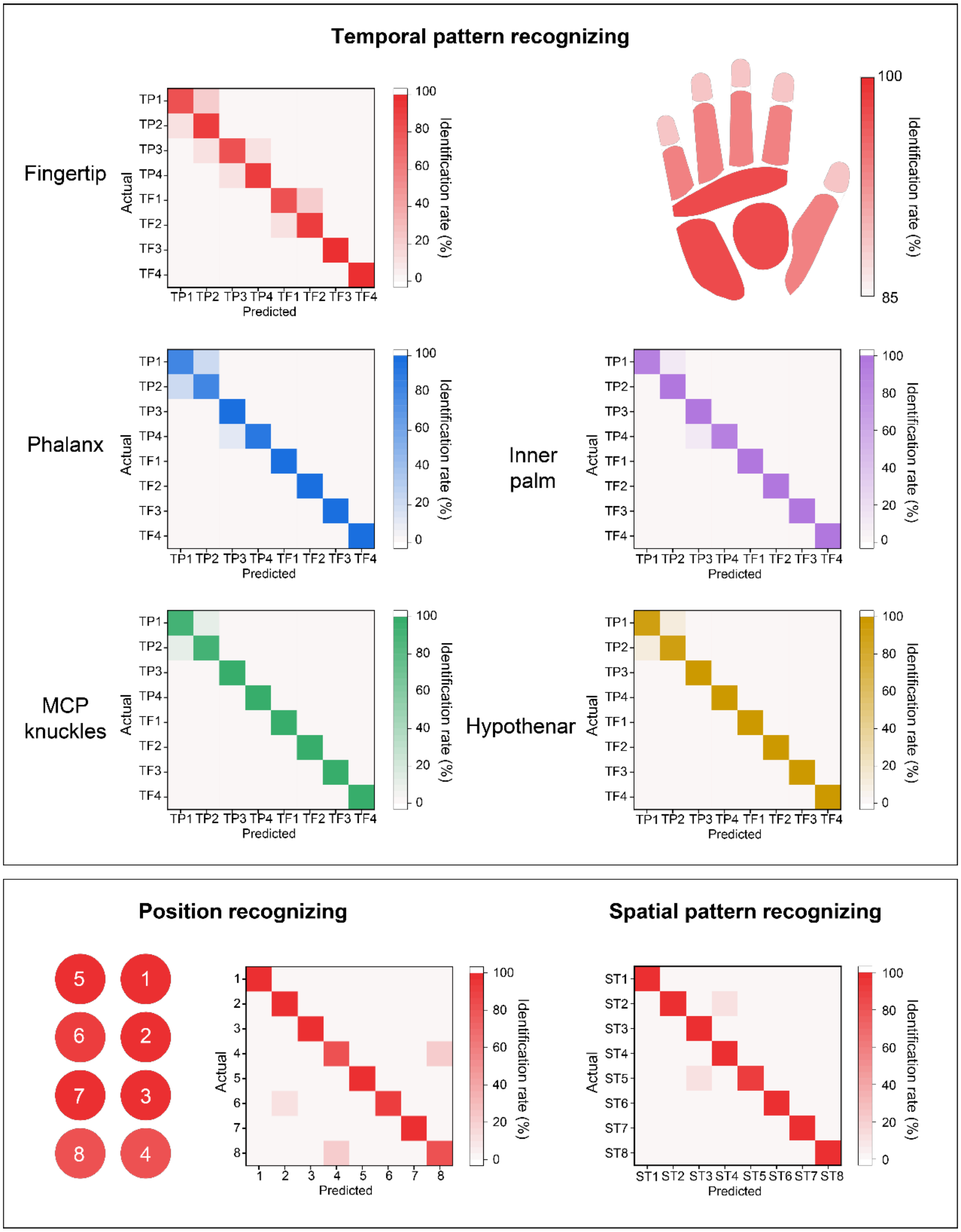

Fig. S23. Individual recognition results. (Volunteer #1)

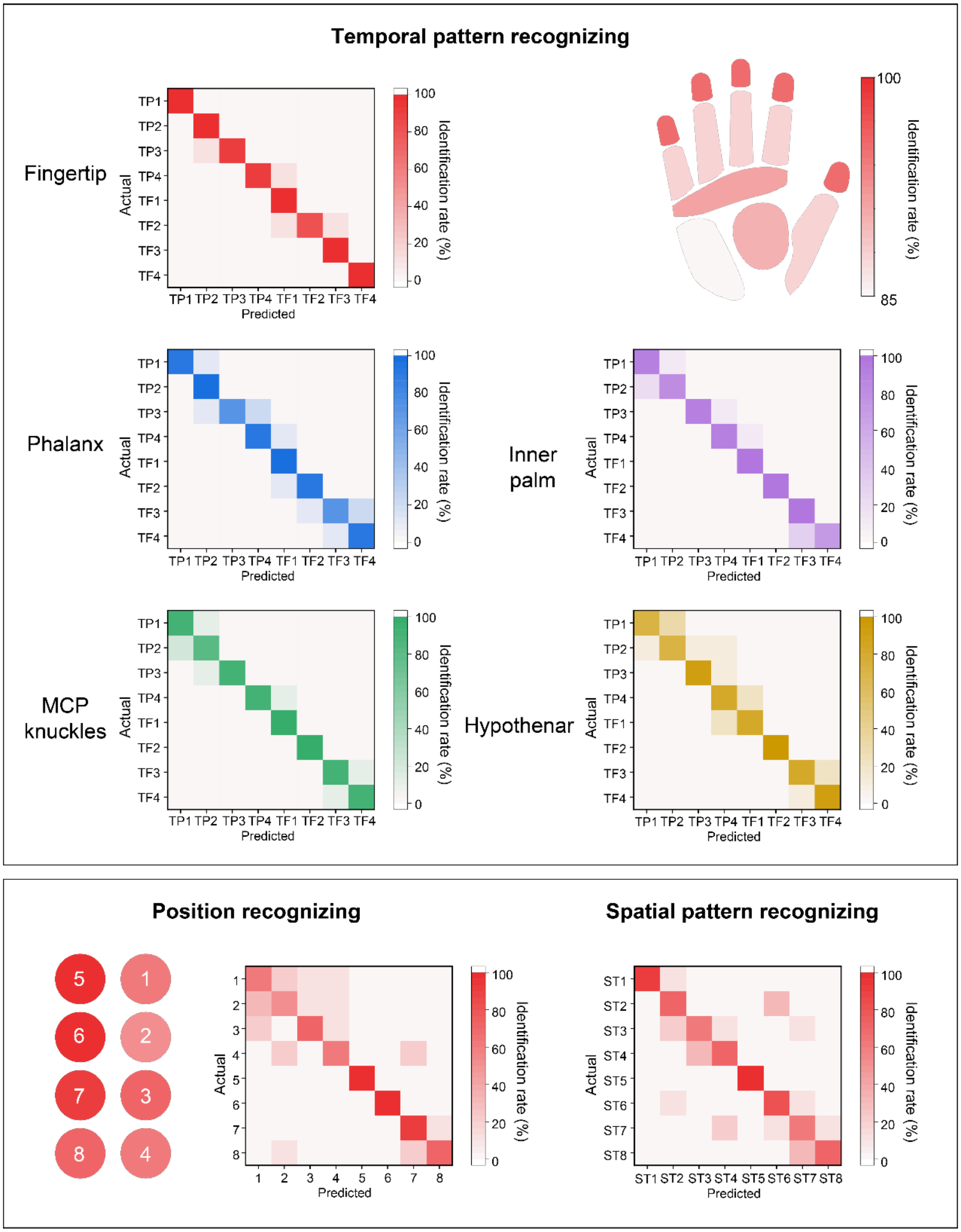
Temporal pattern recognizing

Position recognizing

Spatial pattern recognizing

Fig. S24. Individual recognition results. (Volunteer #2)

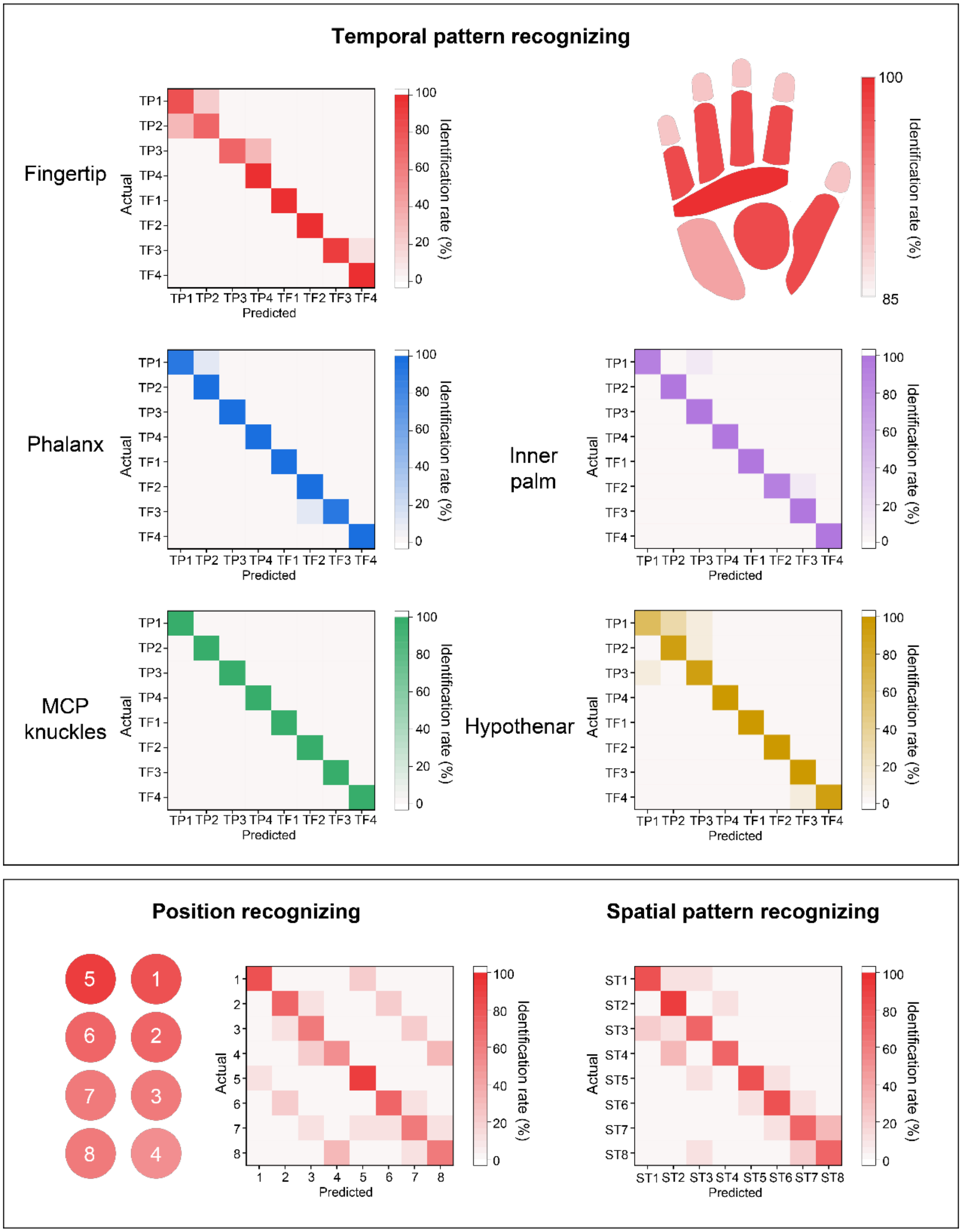

Fig. S25. Individual recognition results. (Volunteer #3)

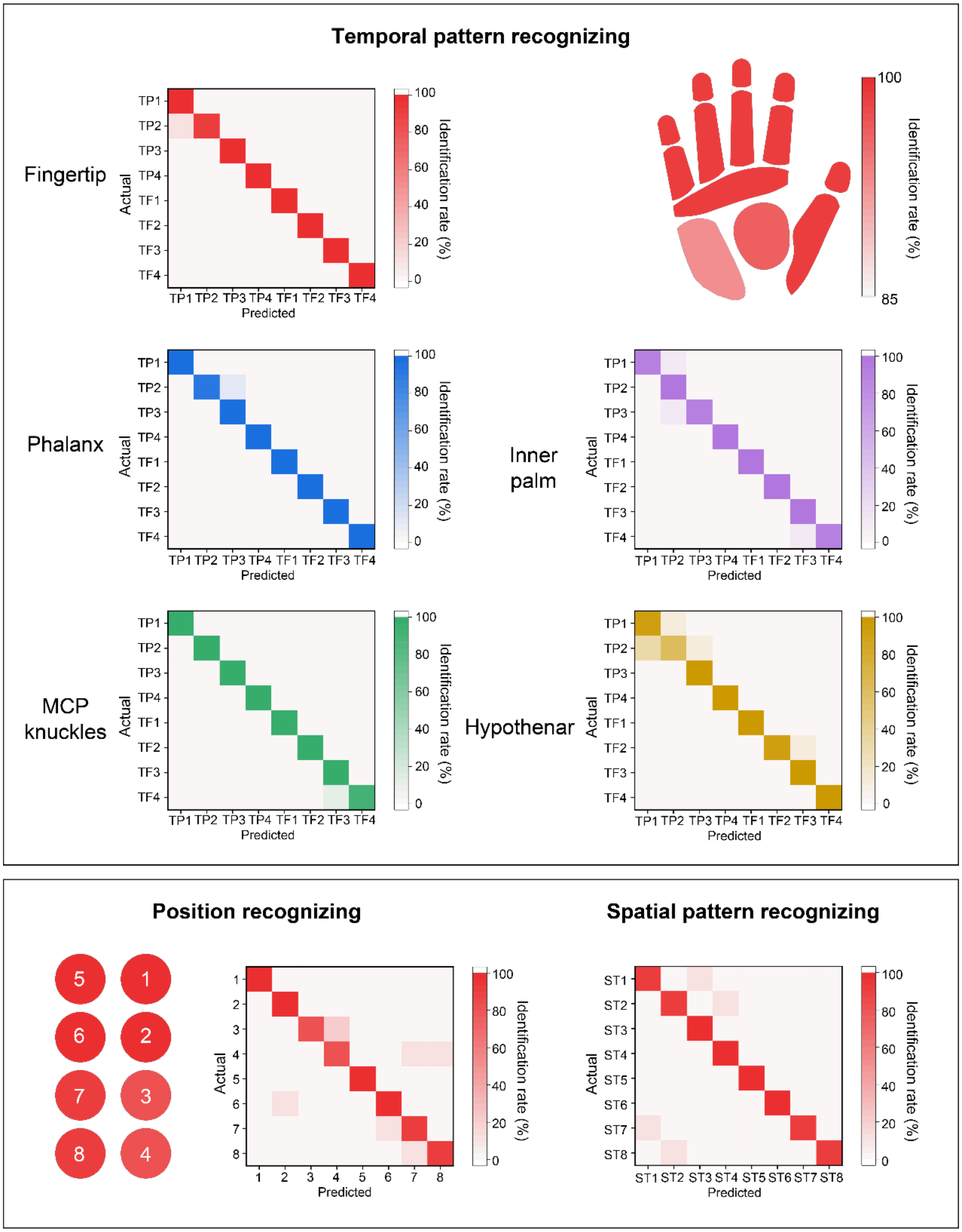
Temporal pattern recognizing

Position recognizing

Spatial pattern recognizing

Fig. S26. Individual recognition results. (Volunteer #4)

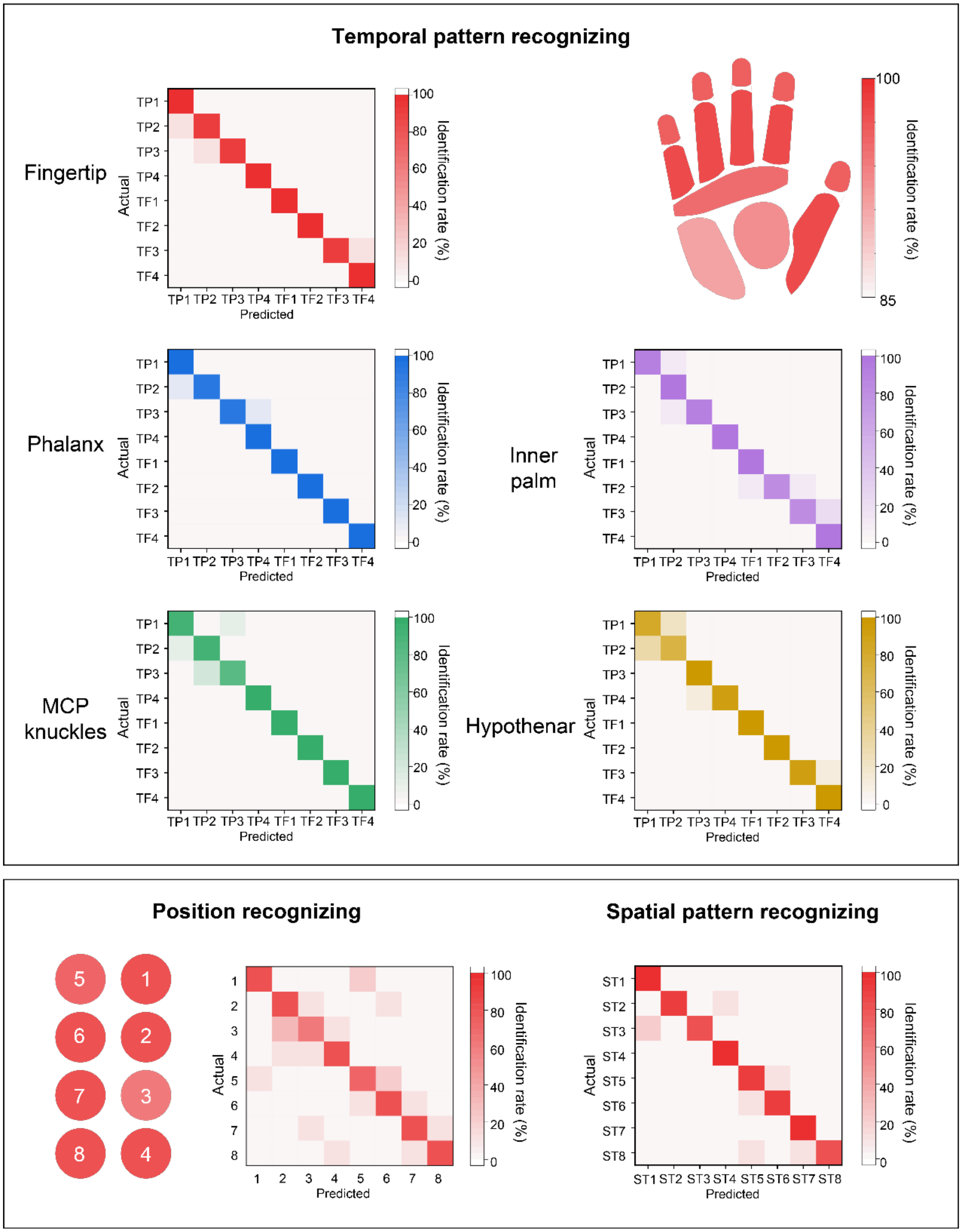

Fig. S27. Individual recognition results. (Volunteer #5)

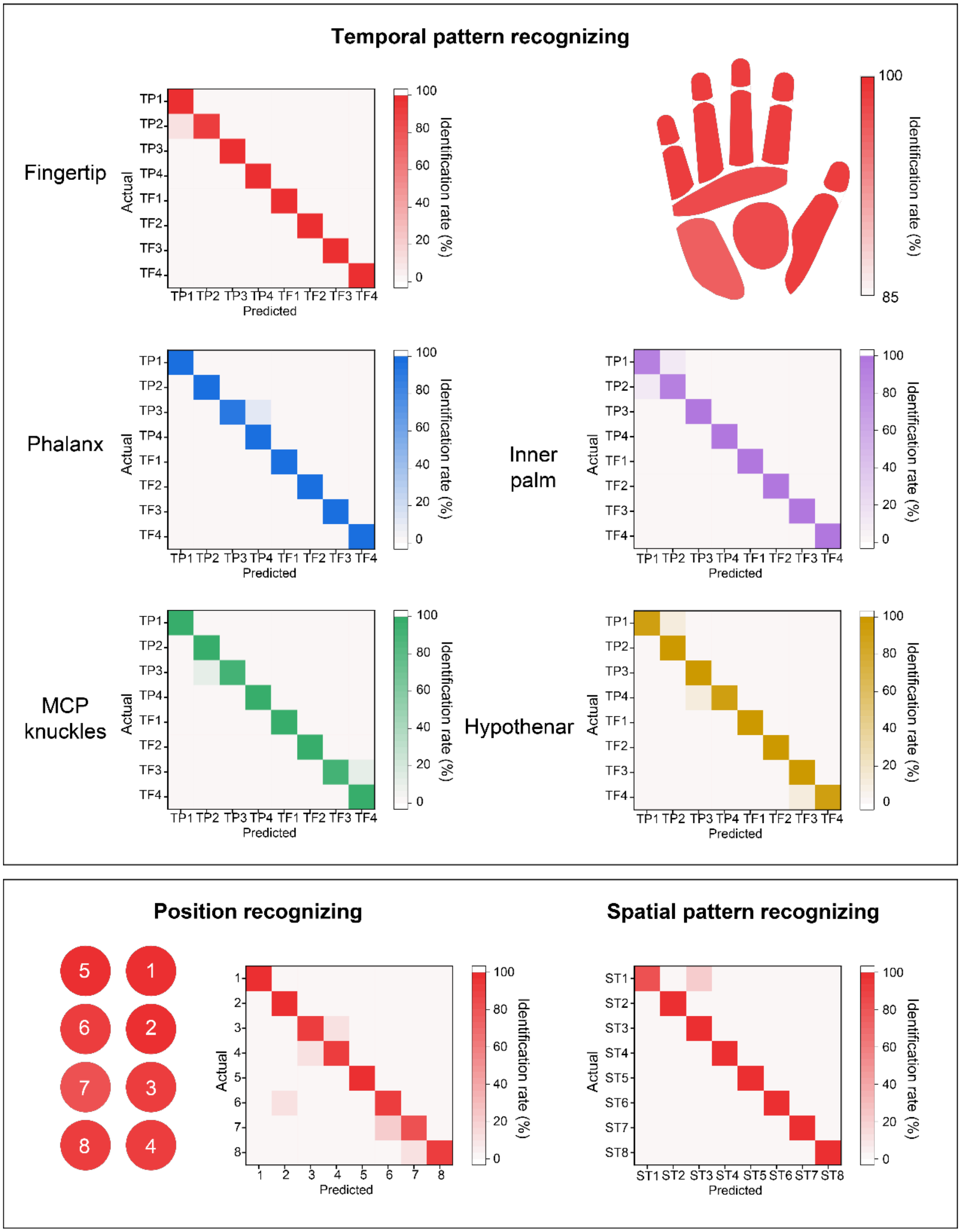

Fig. S28. Individual recognition results. (Volunteer #6)

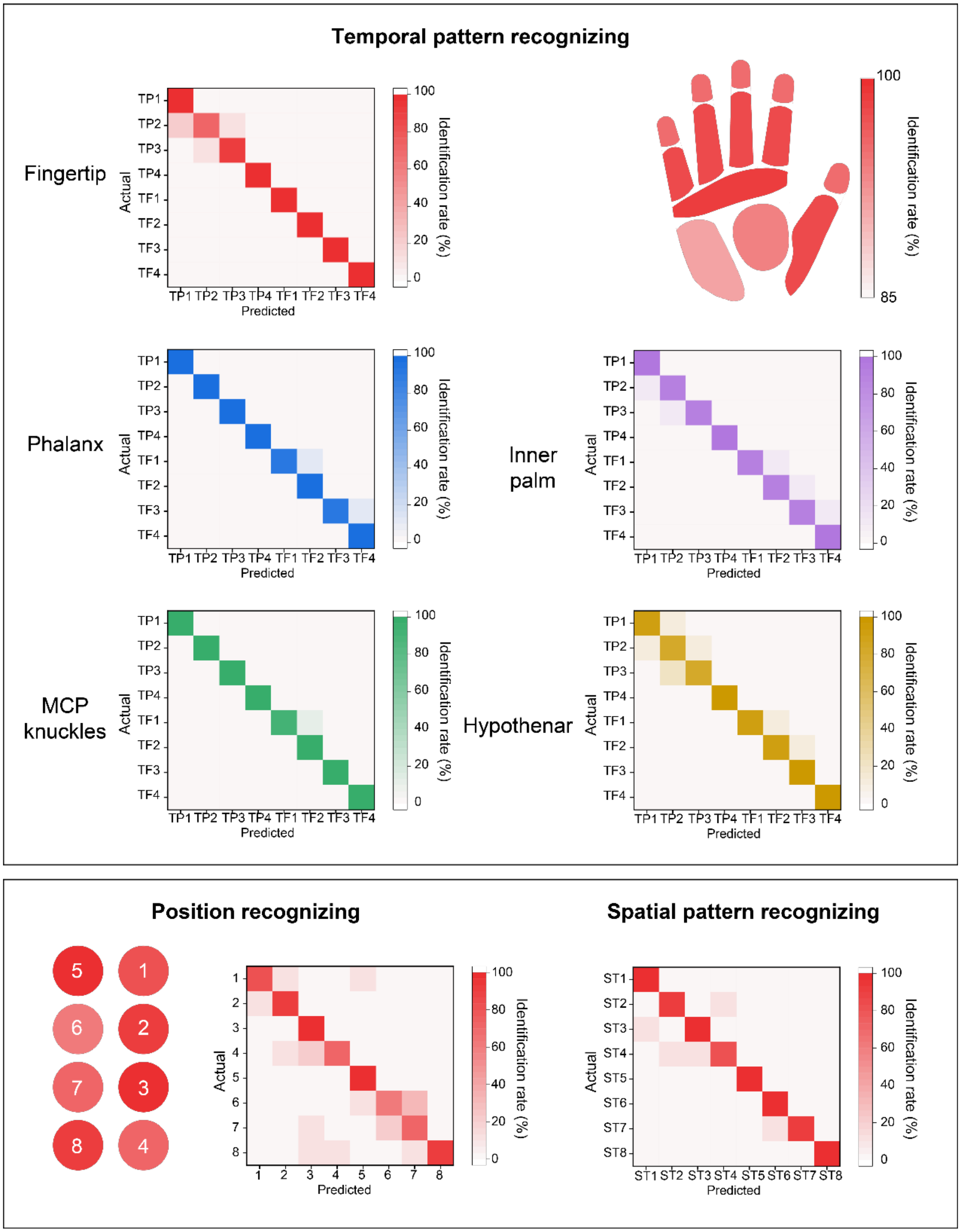

Fig. S29. Individual recognition results. (Volunteer #7)

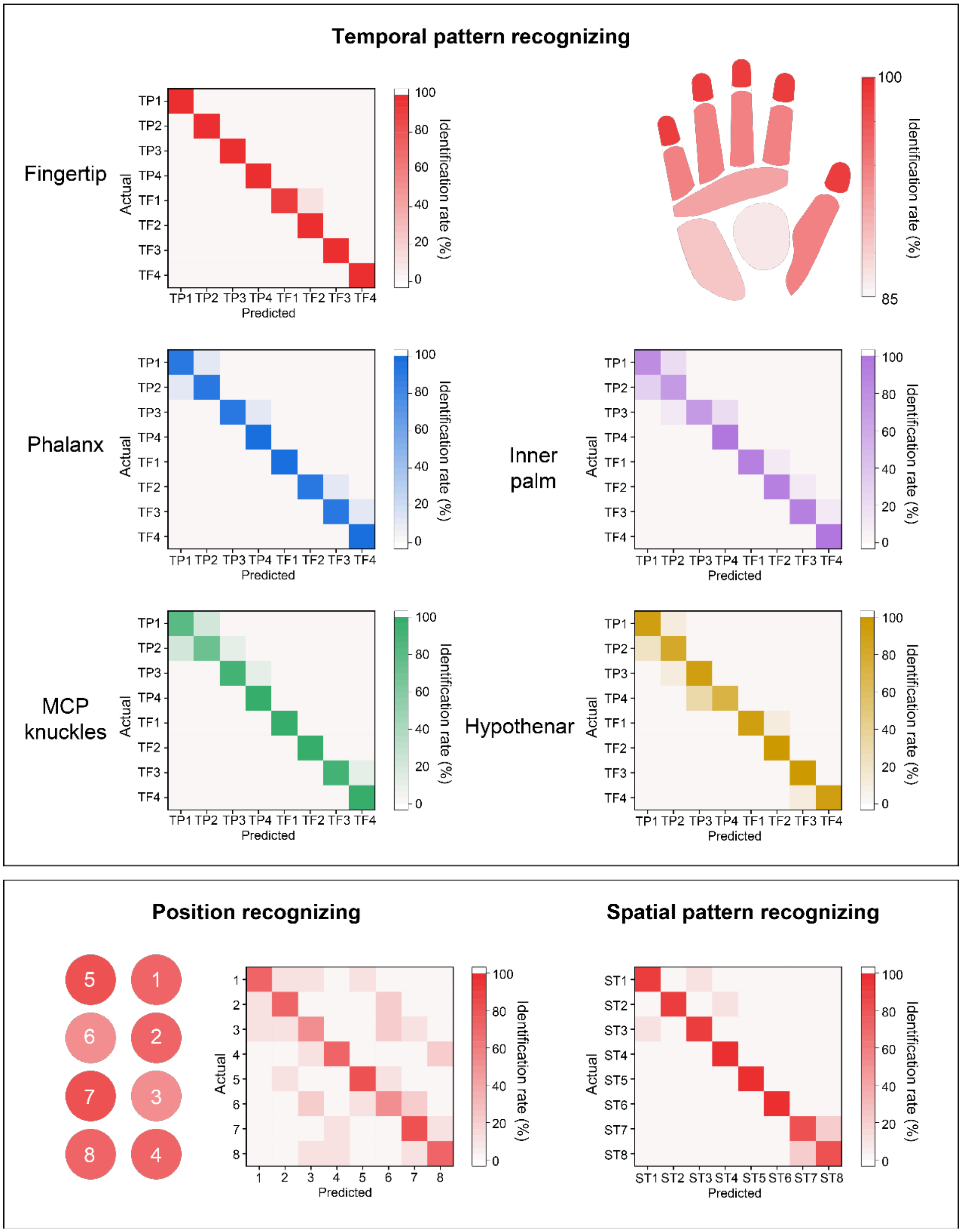

Fig. S30. Individual recognition results. (Volunteer #8)

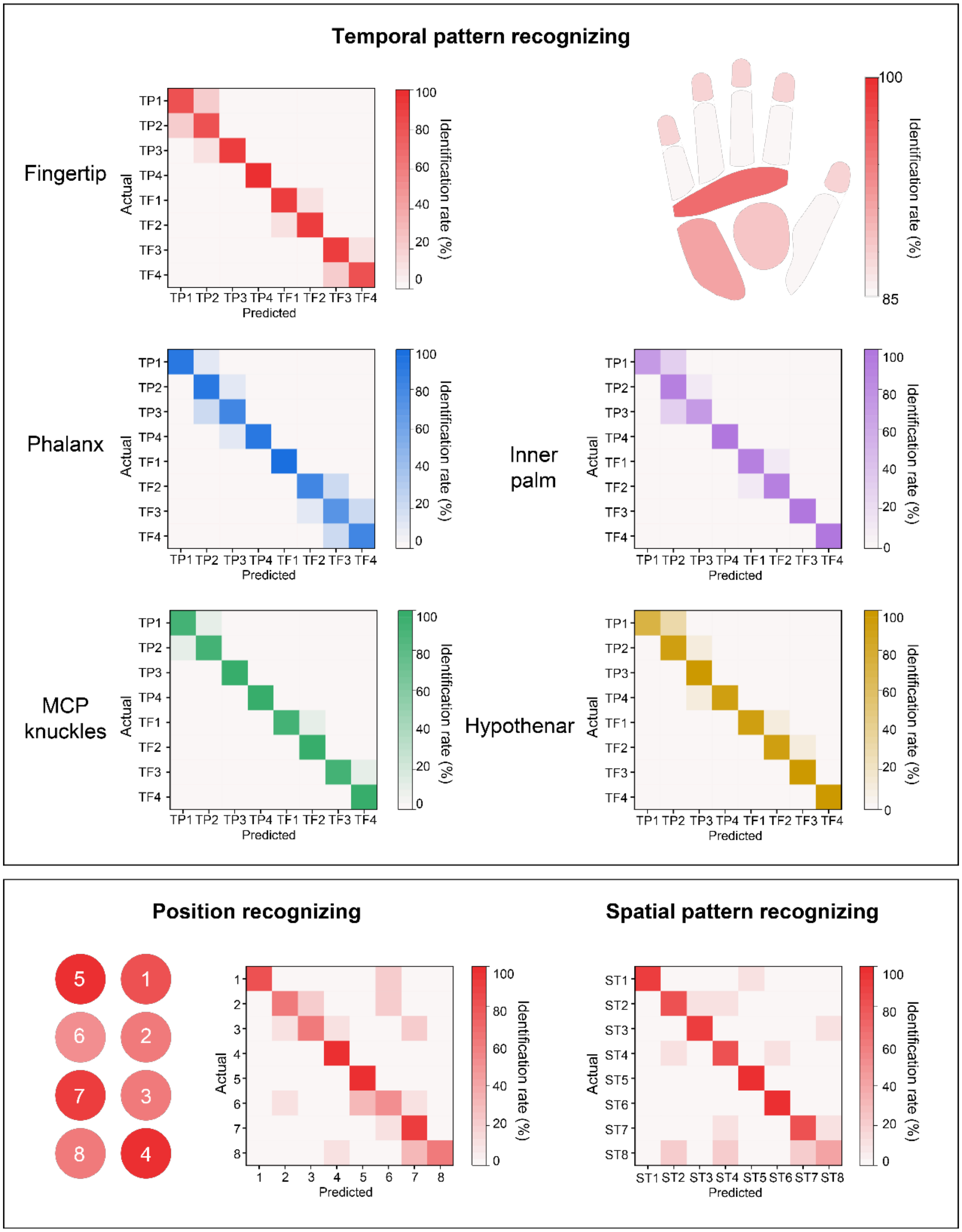

Fig. S31. Individual recognition results. (Volunteer #9)

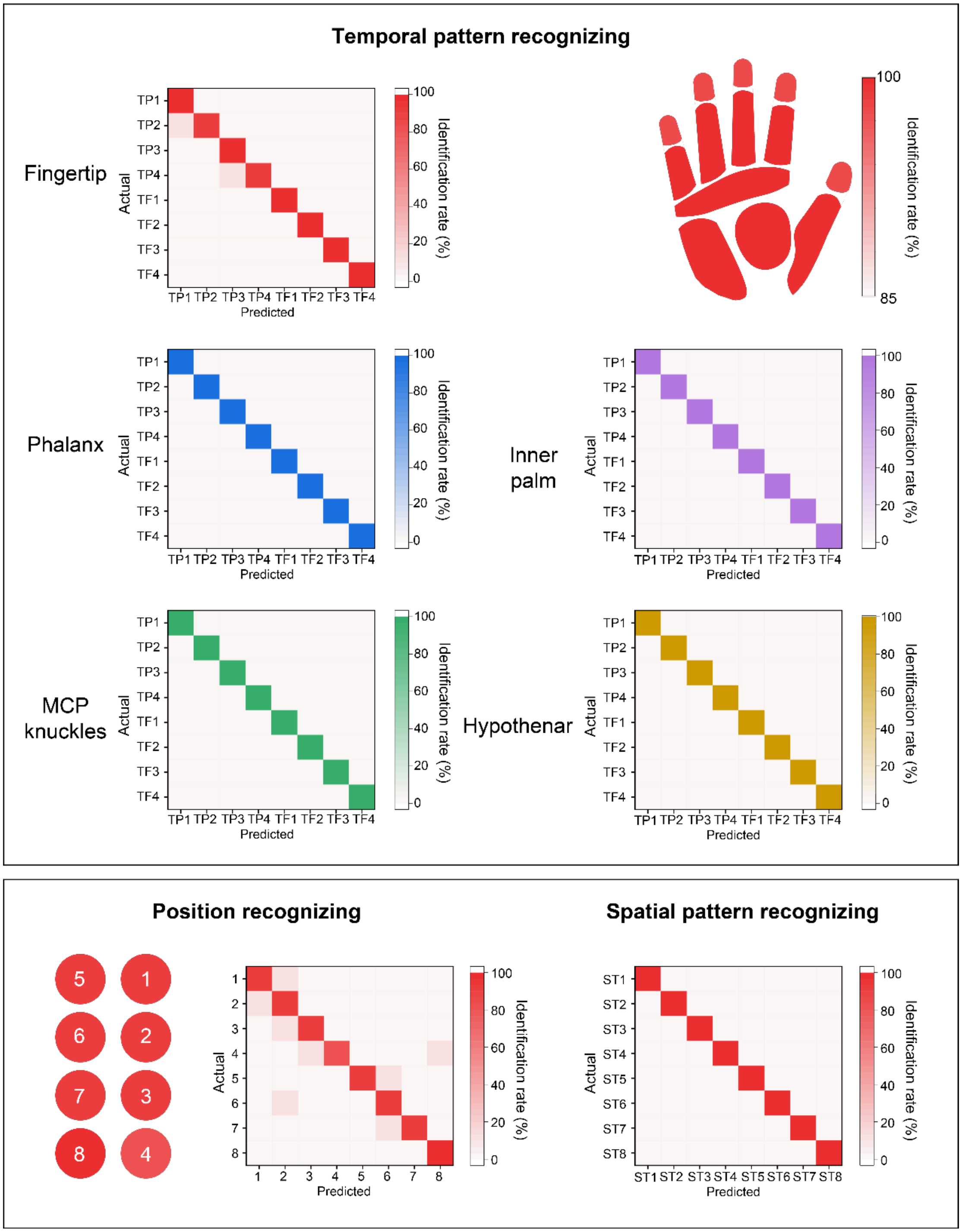

Temporal pattern recognizing

Position recognizing

Spatial pattern recognizing

Fig. S32. Individual recognition results. (Volunteer #10)

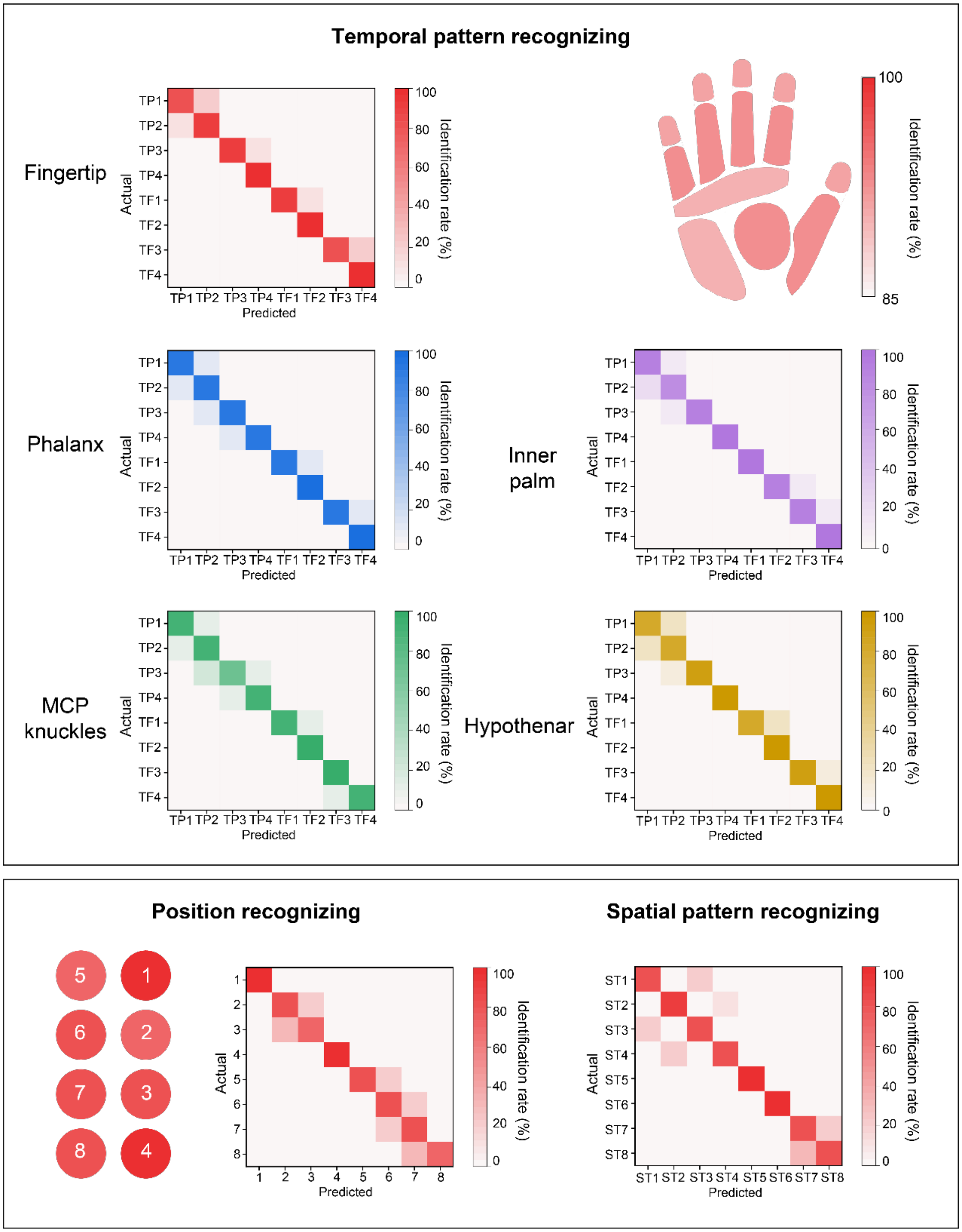

Fig. S33. Individual recognition results. (Volunteer #11)

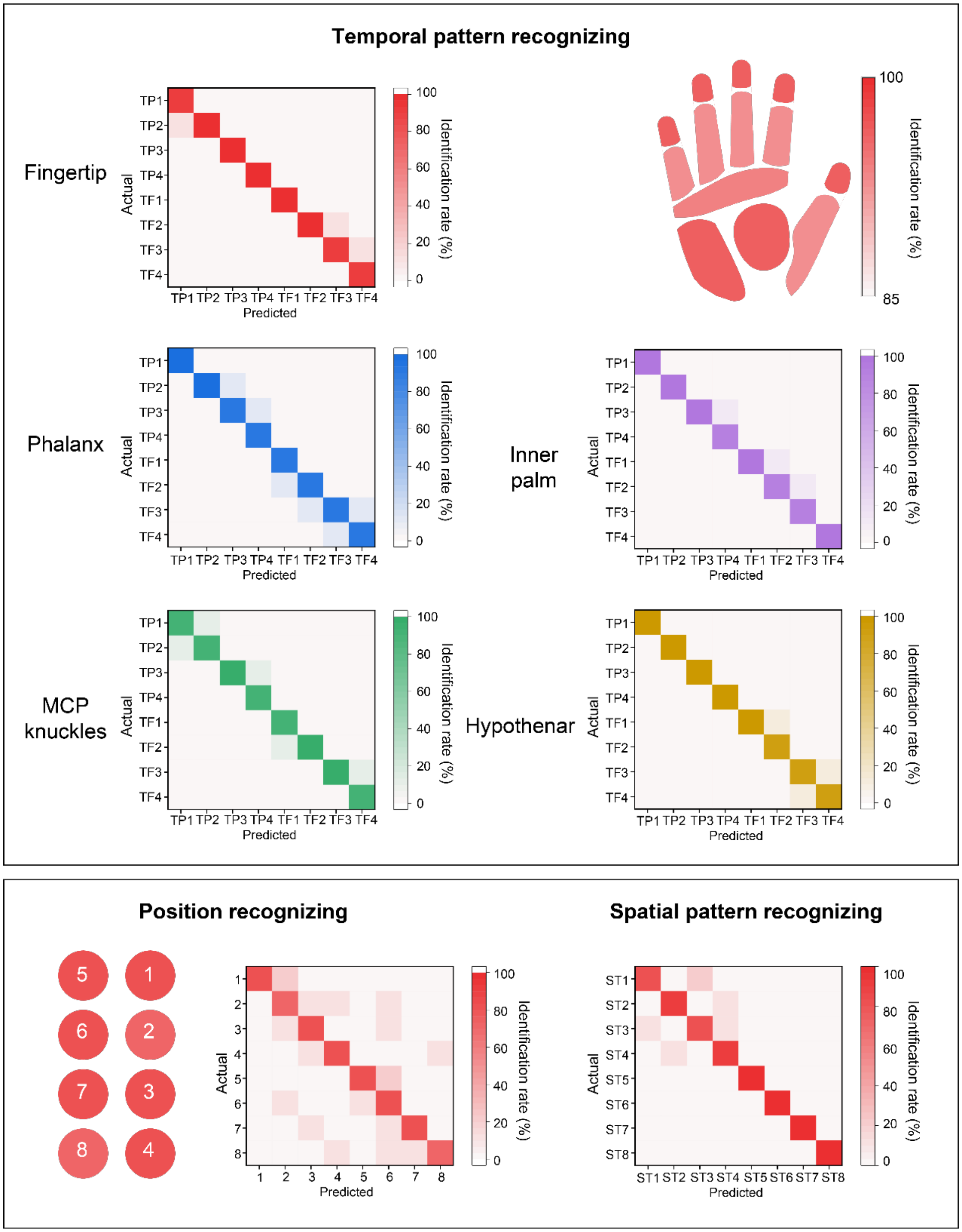

Temporal pattern recognizing

Position recognizing

Spatial pattern recognizing

Fig. S34. Individual recognition results. (Volunteer #12)

Movie S1.
Wearing process of the FIBHT system.

Movie S2.
Rain test for validating the waterproof performance.

Movie S3.
VR scenario where user perceives feedback from FIBHT for recognizing Mahjong tiles.

Movie S4.
VR scenario where user perceives feedback from FIBHT for dynamic gripping in a tennis game.

Movie S5.
FIBHT adheres firmly to the hand in two conditions. 1, just being worn on and 2, exercising after a 30-minute wearing.

REFERENCES AND NOTES

1. A. B. Vallbo, R. S. Johansson, Properties of cutaneous mechanoreceptors in the human hand related to touch sensation. *Hum. Neurobiol.* **3**, 3–14 (1984).

2. Y. Huang, K. Yao, J. Li, D. Li, H. Jia, Y. Liu, C. K. Yiu, W. Park, X. Yu, Recent advances in multi-mode haptic feedback technologies towards wearable interfaces. *Mater. Today Phys.* **22**, 100602 (2022).

3. Y. H. Jung, J.-H. Kim, J. A. Rogers, Skin-integrated vibrohaptic interfaces for virtual and augmented reality. *Adv. Funct. Mater.* **31**, 2008805 (2021).

4. D.-H. Kim, N. Lu, R. Ma, Y.-S. Kim, R.-H. Kim, S. Wang, J. Wu, S. M. Won, H. Tao, A. Islam, K. J. Yu, T. Kim, R. Chowdhury, M. Ying, L. Xu, M. Li, H.-J. Chung, H. Keum, M. McCormick, P. Liu, Y.-W. Zhang, F. G. Omenetto, Y. Huang, T. Coleman, J. A. Rogers, Epidermal electronics. *Science* **333**, 838–843 (2011).

5. Y. Zhao, B. Wang, J. Tan, H. Yin, R. Huang, J. Zhu, S. Lin, Y. Zhou, D. Jelinek, Z. Sun, K. Youssef, L. Voisin, A. Horrillo, K. Zhang, B. M. Wu, H. A. Coller, D. C. Lu, Q. Pei, S. Emaminejad, Soft strain-insensitive bioelectronics featuring brittle materials. *Science* **378**, 1222–1227 (2022).

6. Y. Jiang, S. Ji, J. Sun, J. Huang, Y. Li, G. Zou, T. Salim, C. Wang, W. Li, H. Jin, J. Xu, S. Wang, T. Lei, X. Yan, W. Y. X. Peh, S.-C. Yen, Z. Liu, M. Yu, H. Zhao, Z. Lu, G. Li, H. Gao, Z. Liu, Z. Bao, X. Chen, A universal interface for plug-and-play assembly of stretchable devices. *Nature* **614**, 456–462 (2023).

7. T. Someya, Z. Bao, G. G. Malliaras, The rise of plastic bioelectronics. *Nature* **540**, 379–385 (2016).

8. H. Hu, H. Huang, M. Li, X. Gao, L. Yin, R. Qi, R. S. Wu, X. Chen, Y. Ma, K. Shi, C. Li, T. M. Maus, B. Huang, C. Lu, M. Lin, S. Zhou, Z. Lou, Y. Gu, Y. Chen, Y. Lei, X. Wang, R. Wang, W. Yue, X. Yang, Y. Bian, J. Mu, G. Park, S. Xiang, S. Cai, P. W. Corey, J. Wang, S. Xu, A wearable cardiac ultrasound imager. *Nature* **613**, 667–675 (2023).

9. W. Gao, S. Emaminejad, H. Y. Y. Nyein, S. Challa, K. Chen, A. Peck, H. M. Fahad, H. Ota, H. Shiraki, D. Kiriya, D.-H. Lien, G. A. Brooks, R. W. Davis, A. Javey, Fully integrated wearable sensor arrays for multiplexed in situ perspiration analysis. *Nature* **529**, 509–514 (2016).

10. D. Jung, C. Lim, H. J. Shim, Y. Kim, C. Park, J. Jung, S. I. Han, S.-H. Sunwoo, K. W. Cho, G. D. Cha, D. C. Kim, J. H. Koo, J. H. Kim, T. Hyeon, D.-H. Kim, Highly conductive and elastic nanomembrane for skin electronics. *Science* **373**, 1022–1026 (2021).

11. W. Yang, S. Lin, W. Gong, R. Lin, C. Jiang, X. Yang, Y. Hu, J. Wang, X. Xiao, K. Li, Y. Li, Q. Zhang, J. S. Ho, Y. Liu, C. Hou, H. Wang, Single body-coupled fiber enables chipless textile electronics. *Science* **384**, 74–81 (2024).

12. Y. Liu, C. Yiu, H. Jia, T. Wong, K. Yao, Y. Huang, J. Zhou, X. Huang, L. Zhao, D. Li, M. Wu, Z. Gao, J. He, E. Song, X. Yu, Thin, soft, garment-integrated triboelectric nanogenerators for energy harvesting and human machine interfaces. *EcoMat* **3**, e12123 (2021).

13. J. Xue, Y. Zou, Y. Deng, Z. Li, Bioinspired sensor system for health care and human-machine interaction. *EcoMat* **4**, e12209 (2022).

14. J. Qi, F. Gao, G. Sun, J. C. Yeo, C. T. Lim, HaptGlove—Untethered pneumatic glove for multimode haptic feedback in reality–Virtuality continuum. *Adv. Sci.* **10**, 2301044 (2023).

15. X. Yu, Z. Xie, Y. Yu, J. Lee, A. Vazquez-Guardado, H. Luan, J. Ruban, X. Ning, A. Akhtar, D. Li, B. Ji, Y. Liu, R. Sun, J. Cao, Q. Huo, Y. Zhong, C. Lee, S. Kim, P. Gutruf, C. Zhang, Y. Xue, Q. Guo, A. Chempakasseril, P. Tian, W. Lu, J. Jeong, Y. Yu, J. Cornman, C. Tan, B. Kim, K. Lee, X. Feng, Y. Huang, J. A. Rogers, Skin-integrated wireless haptic interfaces for virtual and augmented reality. *Nature* **575**, 473–479 (2019).

16. Y. Liu, C. Yiu, Z. Song, Y. Huang, K. Yao, T. Wong, J. Zhou, L. Zhao, X. Huang, S. K. Nejad, M. Wu, D. Li, J. He, X. Guo, J. Yu, X. Feng, Z. Xie, X. Yu, Electronic skin as wireless human-machine interfaces for robotic VR. *Sci. Adv.* **8**, eabl6700 (2022).

17. Y. Liu, C. K. Yiu, Z. Zhao, S. Liu, X. Huang, W. Park, J. Su, J. Zhou, T. H. Wong, K. Yao, L. Zhao, Y. Huang, J. Li, P. Fan, B. Zhang, Y. Dai, Z. Yang, Y. Li, X. Yu, Skin-integrated haptic

interfaces enabled by scalable mechanical actuators for virtual reality. *IEEE Internet Things J.* **10**, 653–663 (2023).

18. D. Li, J. Zhou, K. Yao, S. Liu, J. He, J. Su, Q. Qu, Y. Gao, Z. Song, C. Yiu, C. Sha, Z. Sun, B. Zhang, J. Li, L. Huang, C. Xu, T. H. Wong, X. Huang, J. Li, R. Ye, L. Wei, Z. Zhang, X. Guo, Y. Dai, Z. Xie, X. Yu, Touch IoT enabled by wireless self-sensing and haptic-reproducing electronic skin. *Sci. Adv.* **8**, eade2450 (2022).

19. D. Li, J. He, Z. Song, K. Yao, M. Wu, H. Fu, Y. Liu, Z. Gao, J. Zhou, L. Wei, Z. Zhang, Y. Dai, Z. Xie, X. Yu, Miniaturization of mechanical actuators in skin-integrated electronics for haptic interfaces. *Microsyst. Nanoeng.* **7**, 85 (2021).

20. Y. H. Jung, J.-Y. Yoo, A. Vázquez-Guardado, J.-H. Kim, J.-T. Kim, H. Luan, M. Park, J. Lim, H.-S. Shin, C.-J. Su, R. Schloen, J. Trueb, R. Avila, J.-K. Chang, D. S. Yang, Y. Park, H. Ryu, H.-J. Yoon, G. Lee, H. Jeong, J. U. Kim, A. Akhtar, J. Cornman, T. Kim, Y. Huang, J. A. Rogers, A wireless haptic interface for programmable patterns of touch across large areas of the skin. *Nat. Electron.* **5**, 374–385 (2022).

21. Z. Sun, Z. Zhang, C. Lee, A skin-like multimodal haptic interface. *Nat. Electron.* **6**, 941–942 (2023).

22. K. Yao, J. Zhou, Q. Huang, M. Wu, C. K. Yiu, J. Li, X. Huang, D. Li, J. Su, S. Hou, Y. Liu, Y. Huang, Z. Tian, J. Li, H. Li, R. Shi, B. Zhang, J. Zhu, T. H. Wong, H. Jia, Z. Gao, Y. Gao, Y. Zhou, W. Park, E. Song, M. Han, H. Zhang, J. Yu, L. Wang, W. J. Li, X. Yu, Encoding of tactile information in hand via skin-integrated wireless haptic interface. *Nat. Mach. Intell.* **4**, 893–903 (2022).

23. A. Akhtar, J. Sombeck, B. Boyce, T. Bretl, Controlling sensation intensity for electrotactile stimulation in human-machine interfaces. *Sci. Robot.* **3**, eaap9770 (2018).

24. Y. Shi, F. Wang, J. Tian, S. Li, E. Fu, J. Nie, R. Lei, Y. Ding, X. Chen, Z. L. Wang, Self-powered electro-tactile system for virtual tactile experiences. *Sci. Adv.* **7**, eabe2943 (2021).

25. Y. Suga, M. Miyakami, I. Mizoguchi, H. Kajimoto, “3D shape presentation by combination of force feedback and electro-tactile stimulation,” in *2023 IEEE World Haptics Conference (WHC)* (IEEE, 2023), pp. 361–367. https://ieeexplore.ieee.org/abstract/document/10224481/references#references.

26. B. Xu, A. Akhtar, Y. Liu, H. Chen, W.-H. Yeo, S. I. Park, B. Boyce, H. Kim, J. Yu, H.-Y. Lai, S. Jung, Y. Zhou, J. Kim, S. Cho, Y. Huang, T. Bretl, J. A. Rogers, An epidermal stimulation and sensing platform for sensorimotor prosthetic control, management of lower back exertion, and electrical muscle activation. *Adv. Mater.* **28**, 4462–4471 (2016).

27. A. Withana, D. Groeger, J. Steimle, “Tacttoo: A thin and feel-through tattoo for on-skin tactile output” in *Proceedings of the 31st Annual ACM Symposium on User Interface Software and Technology* (Association for Computing Machinery, New York, NY, USA, 2018; *UIST ‘18*, pp. 365–378.

28. M. Ying, A. P. Bonifas, N. Lu, Y. Su, R. Li, H. Cheng, A. Ameen, Y. Huang, J. A. Rogers, Silicon nanomembranes for fingertip electronics. *Nanotechnology* **23**, 344004 (2012).

29. G. Gu, N. Zhang, H. Xu, S. Lin, Y. Yu, G. Chai, L. Ge, H. Yang, Q. Shao, X. Sheng, X. Zhu, X. Zhao, A soft neuroprosthetic hand providing simultaneous myoelectric control and tactile feedback. *Nat. Biomed. Eng.* **7**, 589–598 (2023).

30. Z. Zhang, Z. Xu, L. Emu, P. Wei, S. Chen, Z. Zhai, L. Kong, Y. Wang, H. Jiang, Active mechanical haptics with high-fidelity perceptions for immersive virtual reality. *Nat. Mach. Intell.* **5**, 643–655 (2023).

31. M. Smith, V. Cacucciolo, H. Shea, Fiber pumps for wearable fluidic systems. *Science* **379**, 1327–1332 (2023).

32. J. Oh, S. Kim, S. Lee, S. Jeong, S. H. Ko, J. Bae, A liquid metal based multimodal sensor and haptic feedback device for thermal and tactile sensation generation in virtual reality. *Adv. Funct. Mater.* **31**, 2007772 (2021).

33. R. L. Peiris, Y.-L. Feng, L. Chan, K. Minamizawa, “ThermalBracelet: Exploring thermal haptic feedback around the wrist,” in *Proceedings of the 2019 CHI Conference on Human Factors in Computing Systems* (Association for Computing Machinery, New York, NY, USA, 2019); *CHI ‘19*, pp. 1–11.

34. Y. Huang, J. Zhou, P. Ke, X. Guo, C. K. Yiu, K. Yao, S. Cai, D. Li, Y. Zhou, J. Li, T. H. Wong, Y. Liu, L. Li, Y. Gao, X. Huang, H. Li, J. Li, B. Zhang, Z. Chen, H. Zheng, X. Yang, H. Gao, Z. Zhao, X. Guo, E. Song, H. Wu, Z. Wang, Z. Xie, K. Zhu, X. Yu, A skin-integrated multimodal haptic interface for immersive tactile feedback. *Nat. Electron.* **6**, 1020–1031 (2023).

35. H. Zhai, H. I. Maibach, Skin occlusion and irritant and allergic contact dermatitis: An overview. *Contact Dermatitis* **44**, 201–206 (2001).

36. B. Zhang, J. Li, J. Zhou, L. Chow, G. Zhao, Y. Huang, Z. Ma, Q. Zhang, Y. Yang, C. K. Yiu, J. Li, F. Chun, X. Huang, Y. Gao, P. Wu, S. Jia, H. Li, D. Li, Y. Liu, K. Yao, R. Shi, Z. Chen, B. L. Khoo, W. Yang, F. Wang, Z. Zheng, Z. Wang, X. Yu, A three-dimensional liquid diode for soft, integrated permeable electronics. *Nature* **628**, 84–92 (2024).

37. S. J. Park, T. Tamura, Distribution of evaporation rate on human body surface. *Ann. Physiol. Anthropol.* **11**, 593–609 (1992).

38. J. Kaiser, A. D. Nimbarte, D. Davari, B. Gopalakrishnan, X. He, Study of skin conductance and perceived discomfort of the hand/finger system under controlled atmospheric conditions. *Theor. Issues Ergon. Sci.* **18**, 442–454 (2017).

39. Z. Ma, Q. Huang, Q. Xu, Q. Zhuang, X. Zhao, Y. Yang, H. Qiu, Z. Yang, C. Wang, Y. Chai, Z. Zheng, Permeable superelastic liquid-metal fibre mat enables biocompatible and monolithic stretchable electronics. *Nat. Mater.* **20**, 859–868 (2021).

40. Q. Zhuang, K. Yao, M. Wu, Z. Lei, F. Chen, J. Li, Q. Mei, Y. Zhou, Q. Huang, X. Zhao, Y. Li, X. Yu, Z. Zheng, Wafer-patterned, permeable, and stretchable liquid metal microelectrodes for implantable bioelectronics with chronic biocompatibility. *Sci. Adv.* **9**, eadg8602 (2023).

41. Z. Huang, Y. Hao, Y. Li, H. Hu, C. Wang, A. Nomoto, T. Pan, Y. Gu, Y. Chen, T. Zhang, W. Li, Y. Lei, N. Kim, C. Wang, L. Zhang, J. W. Ward, A. Maralani, X. Li, M. F. Durstock, A. Pisano, Y. Lin, S. Xu, Three-dimensional integrated stretchable electronics. *Nat. Electron.* **1**, 473–480 (2018).

42. Q. Zhuang, K. Yao, C. Zhang, X. Song, J. Zhou, Y. Zhang, Q. Huang, Y. Zhou, X. Yu, Z. Zheng, Permeable, three-dimensional integrated electronic skins with stretchable hybrid liquid metal solders. *Nat. Electron.* **7**, 598–609 (2024).

43. J. C. Yeo, Z. Liu, Z.-Q. Zhang, P. Zhang, Z. Wang, C. T. Lim, Wearable mechanotransduced tactile sensor for haptic perception. *Adv. Mater. Technol.* **2**, 1700006 (2017).

44. M. D. Dickey, R. C. Chiechi, R. J. Larsen, E. A. Weiss, D. A. Weitz, G. M. Whitesides, Eutectic gallium-indium (EGaIn): A liquid metal alloy for the formation of stable structures in microchannels at room temperature. *Adv. Funct. Mater.* **18**, 1097–1104 (2008).

45. K. Nan, S. Babaee, W. W. Chan, J. L. P. Kuosmanen, V. R. Feig, Y. Luo, S. S. Srinivasan, C. M. Patterson, A. M. Jebran, G. Traverso, Low-cost gastrointestinal manometry via silicone–liquid-metal pressure transducers resembling a quipu. *Nat. Biomed. Eng.* **6**, 1092–1104 (2022).

46. F. Chen, Q. Zhuang, Y. Ding, C. Zhang, X. Song, Z. Chen, Y. Zhang, Q. Mei, X. Zhao, Q. Huang, Z. Zheng, Wet-adaptive electronic skin. *Adv. Mater.* **35**, 2305630 (2023).

47. C. Wang, X. Chen, L. Wang, M. Makihata, H.-C. Liu, T. Zhou, X. Zhao, Bioadhesive ultrasound for long-term continuous imaging of diverse organs. *Science* **377**, 517–523 (2022).

48. H. Choi, Y. Kim, S. Kim, H. Jung, S. Lee, K. Kim, H.-S. Han, J. Y. Kim, M. Shin, D. Son, Adhesive bioelectronics for sutureless epicardial interfacing. *Nat. Electron.* **6**, 779–789 (2023).

49. H. Yuk, J. Wu, X. Zhao, Hydrogel interfaces for merging humans and machines. *Nat. Rev. Mater.* **7**, 935–952 (2022).

50. Q. Huang, Z. Zheng, Pathway to developing permeable electronics. *ACS Nano* **16**, 15537–15544 (2022).

51. M. Bariya, L. Li, R. Ghattamaneni, C. H. Ahn, H. Y. Y. Nyein, L.-C. Tai, A. Javey, Glove-based sensors for multimodal monitoring of natural sweat. *Sci. Adv.* **6**, eabb8308 (2020).

52. J. Yi, G. Zou, J. Huang, X. Ren, Q. Tian, Q. Yu, P. Wang, Y. Yuan, W. Tang, C. Wang, L. Liang, Z. Cao, Y. Li, M. Yu, Y. Jiang, F. Zhang, X. Yang, W. Li, X. Wang, Y. Luo, X. J. Loh, G. Li, B. Hu, Z. Liu, H. Gao, X. Chen, Water-responsive supercontractile polymer films for bioelectronic interfaces. *Nature* **624**, 295–302 (2023).

53. C. Boehler, S. Carli, L. Fadiga, T. Stieglitz, M. Asplund, Tutorial: Guidelines for standardized performance tests for electrodes intended for neural interfaces and bioelectronics. *Nat. Protoc.* **15**, 3557–3578 (2020).

54. J. Deng, H. Yuk, J. Wu, C. E. Varela, X. Chen, E. T. Roche, C. F. Guo, X. Zhao, Electrical bioadhesive interface for bioelectronics. *Nat. Mater.* **20**, 229–236 (2021).

55. Q. Zhang, Y. Yang, D. Suo, S. Zhao, J. C.-W. Cheung, P. H.-M. Leung, X. Zhao, A biomimetic adhesive and robust Janus patch with anti-oxidative, anti-inflammatory, and anti-bacterial activities for tendon repair. *ACS Nano* **17**, 16798–16816 (2023).

56. V. K. Truong, A. Hayles, R. Bright, T. Q. Luu, M. D. Dickey, K. Kalantar-Zadeh, K. Vasilev, Gallium liquid metal: Nanotoolbox for antimicrobial applications. *ACS Nano* **17**, 14406–14423 (2023).

57. Q. Zhang, Y. Luo, B. Liang, D. Suo, S. Lyu, Y. Wang, X. Zhao, An anti-bacterial and anti-cancer fibrous membrane with multiple therapeutic effects for prevention of pancreatic cancer recurrence. *Biomater. Adv.* **137**, 212831 (2022).

58. T. Ahmad, Reviewing the tannic acid mediated synthesis of metal nanoparticles. *J. Nanotechnol.* **2014**, 954206 (2014).

59. A. Baldwin, B. W. Booth, Biomedical applications of tannic acid. *J. Biomater. Appl.* **36**, 1503–1523 (2022).

60. İ. Gülçin, Z. Huyut, M. Elmastaş, H. Y. Aboul-Enein, Radical scavenging and antioxidant activity of tannic acid. *Arab. J. Chem.* **3**, 43–53 (2010).

61. R. Defrin, A. Ohry, N. Blumen, G. Urca, Sensory determinants of thermal pain. *Brain* **125**, 501–510 (2002).

62. N. A. Martin, S. Falder, A review of the evidence for threshold of burn injury. *Burns* **43**, 1624–1639 (2017).

63. R. S. Johansson, A. B. Vallbo, Tactile sensibility in the human hand: Relative and absolute densities of four types of mechanoreceptive units in glabrous skin. *J. Physiol.* **286**, 283–300 (1979).

64. D. S. Louis, T. L. Greene, K. E. Jacobson, C. Rasmussen, P. Kolowich, S. A. Goldstein, Evaluation of normal values for stationary and moving two-point discrimination in the hand. *J. Hand Surg. Am.* **9**, 552–555 (1984).

65. S. Thube, M. R. Shah, P. H. Kothari, V. Shah, Assessment of two point discrimination on hand in adult population: An observational study. *Int. J. Health Sci. Res.* **10**, 60–63 (2020).

66. M. Ganji, A. Tanaka, V. Gilja, E. Halgren, S. A. Dayeh, Scaling effects on the electrochemical stimulation performance of Au, Pt, and PEDOT:PSS electrocorticography arrays. *Adv. Funct. Mater.* **27**, 1703019 (2017).

67. S. Cai, P. Ke, T. Narumi, K. Zhu, "ThermAirGlove: A pneumatic glove for thermal perception and material identification in virtual reality," in *2020 IEEE Conference on Virtual Reality and 3D User Interfaces (VR)* (IEEE, Atlanta, GA, USA, 2020), pp. 248–257. https://ieeexplore.ieee.org/document/9089505/.

68. Y. Tanaka, A. Shen, A. Kong, P. Lopes, "Full-hand electro-tactile feedback without obstructing palmar side of hand," in *Proceedings of the 2023 CHI Conference on Human Factors in Computing Systems* (Association for Computing Machinery, New York, NY, USA, 2023); *CHI '23*, pp. 1–15.

69. C. Cao, H. Liu, Y. Zhang, W. Jia, L. Zhang, H. Bao, A seamless, large-area silk-based interface for immersive on-palm tactile feedback. *Adv. Mater. Technol.* **9**, 2301599 (2024).

70. Y. Luo, C. Liu, Y. J. Lee, J. DelPreto, K. Wu, M. Foshey, D. Rus, T. Palacios, Y. Li, A. Torralba, W. Matusik, Adaptive tactile interaction transfer via digitally embroidered smart gloves. *Nat. Commun.* **15**, 868 (2024).

71. C. V. Keef, L. V. Kayser, S. Tronboll, C. W. Carpenter, N. B. Root, M. Finn III, T. F. O'Connor, S. N. Abuhamdieh, D. M. Davies, R. Runser, Y. S. Meng, V. S. Ramachandran, D. J. Lipomi, Virtual texture generated using elastomeric conductive block copolymer in a wireless multimodal haptic glove. *Adv. Intell. Syst.* **2**, 2000018 (2020).

72. W. Lin, D. Zhang, W. W. Lee, X. Li, Y. Hong, Q. Pan, R. Zhang, G. Peng, H. Z. Tan, Z. Zhang, L. Wei, Z. Yang, Super-resolution wearable electrotactile rendering system. *Sci. Adv.* **8**, eabp8738 (2022).